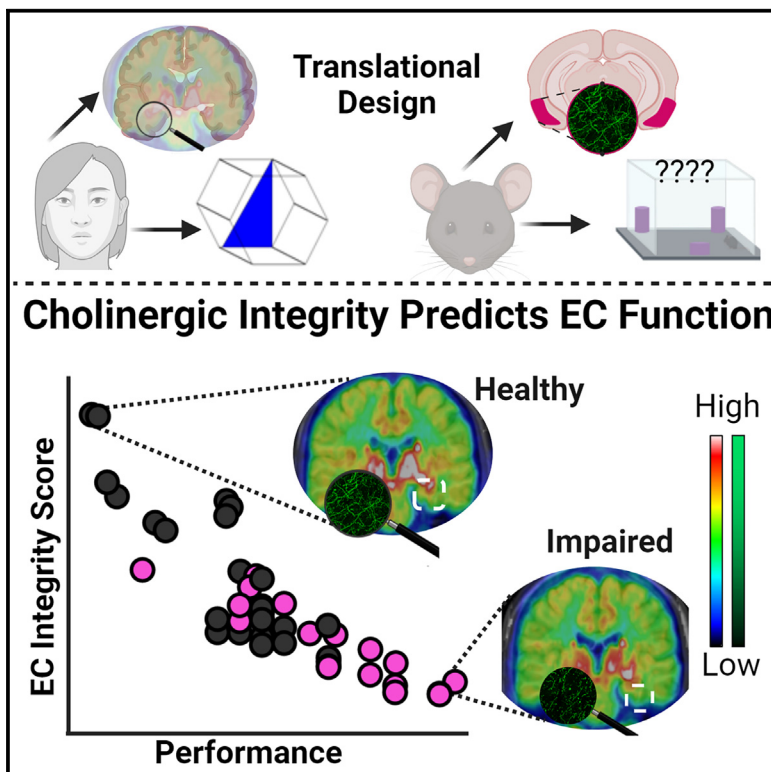


## A central role for acetylcholine in entorhinal cortex function and dysfunction with age in humans and mice

### Graphical abstract



### Authors

Mala R. Ananth, John D. Gardus,  
Chuan Huang, ..., David A. Talmage,  
Christine DeLorenzo, Lorna W. Role

### Correspondence

mala.ananth@nih.gov (M.R.A.),  
lorna.role@nih.gov (L.W.R.)

### In brief

Ananth et al. demonstrate that loss of cholinergic innervation to the entorhinal cortex is an early feature related to cognitive decline. In a series of translational experiments in humans and mice, they establish the importance of cholinergic input in maintaining normal entorhinal cortical function.

### Highlights

- Loss of cholinergic input to entorhinal cortex predicts cognitive decline in mouse and human
- Cholinergic signaling to the entorhinal cortex is required for object location memory
- Loss of function of EC-projecting cholinergic neurons precedes overt cholinergic cell loss
- Early cholinergic vulnerability is conserved between mouse and human



## Article

# A central role for acetylcholine in entorhinal cortex function and dysfunction with age in humans and mice

Mala R. Ananth,<sup>1,8,\*</sup> John D. Gardus,<sup>2</sup> Chuan Huang,<sup>3,4</sup> Nikhil Palekar,<sup>2</sup> Mark Slifstein,<sup>2</sup> Laszlo Zaborszky,<sup>5</sup> Ramin V. Parsey,<sup>2,6</sup> David A. Talmage,<sup>1</sup> Christine DeLorenzo,<sup>2,6,7</sup> and Lorna W. Role<sup>1,7,\*</sup>

<sup>1</sup>National Institute of Neurological Disorders and Stroke, NIH, Bethesda, MD 20892, USA

<sup>2</sup>Department of Psychiatry and Behavioral Health, Stony Brook Medicine, Stony Brook, NY, USA

<sup>3</sup>Department of Radiology and Imaging Sciences, Emory University School of Medicine, Atlanta, GA, USA

<sup>4</sup>Department of Biomedical Engineering, Georgia Institute of Technology and Emory University, Atlanta, GA, USA

<sup>5</sup>Center for Molecular and Behavioral Neuroscience, Rutgers University, New Newark, NJ, USA

<sup>6</sup>Department of Biomedical Engineering, Stony Brook University, Stony Brook, NY, USA

<sup>7</sup>These authors contributed equally

<sup>8</sup>Lead contact

\*Correspondence: [mala.ananth@nih.gov](mailto:mala.ananth@nih.gov) (M.R.A.), [lorna.role@nih.gov](mailto:lorna.role@nih.gov) (L.W.R.)

<https://doi.org/10.1016/j.celrep.2025.115249>

## SUMMARY

Structural and functional changes in the entorhinal cortex (EC) are among the earliest signs of cognitive aging. Here, we ask whether a compromised cholinergic system influences early EC impairments and plays a primary role in EC cognition. We evaluated the relationship between loss of integrity of cholinergic inputs to the EC and cognitive deficits in otherwise healthy humans and mice. Using *in vivo* imaging (PET/MRI) in older humans and high-resolution imaging in wild-type mice and mice with genetic susceptibility to Alzheimer's disease pathology, we establish that loss of cholinergic input to the EC is, in fact, an early feature in cognitive aging. Through mechanistic studies in mice, we find a central role for EC-projecting cholinergic neurons in the expression of EC-related behaviors. Our data demonstrate that alterations to the cholinergic EC are an early, conserved feature of cognitive aging across species and may serve as an early predictor of cognitive status.

## INTRODUCTION

Acetylcholine is a key neuromodulator in the brain that is critical for attention, wakefulness, mood, and memory.<sup>1</sup> Cholinergic neurons (neurons that synthesize and release acetylcholine) coordinate neuronal activity brain-wide to promote attention to salient stimuli and facilitate learning.<sup>2</sup> Basal forebrain cholinergic neurons (BFCNs) span the entire rostrocaudal forebrain and send projections to much of the brain.<sup>3</sup> The broad reach of these projections coupled with their functional organization grants cholinergic neurons highly flexible, context-specific control over cortical dynamics, making a strong case for the functional importance of acetylcholine in cognitive behaviors.<sup>4</sup>

Postmortem analyses reveal loss of BFCNs and fragmentation of cholinergic projections in pathological aging conditions such as Alzheimer's disease (AD).<sup>5–8</sup> What these studies lack is an understanding of when changes to the cholinergic system occur and the importance of these changes to changes in cognition. Addressing these questions requires truly early assessment of the integrity of the cholinergic system.

One of the brain regions earliest affected by age is the entorhinal cortex (EC).<sup>9</sup> The EC serves as the primary input and output structure for the hippocampal formation and thus is essential for

memory.<sup>10,11</sup> Histopathological studies reveal that accumulation of tau pathology associated with AD begins in the *trans*-entorhinal and lateral portions of the EC.<sup>12,13</sup> In addition, structural and functional alterations to the EC precede and are even predictive of future cognitive impairment.<sup>14–18</sup> Functional deficits in the EC, resulting in deficits in object location memory, and processing of complex objects are among the earliest reported in AD progression.<sup>19–21</sup> The EC receives cholinergic input from a cluster of anteriorly positioned BFCNs.<sup>1,3,22</sup> Whether a compromised cholinergic system influences the early cognitive changes in EC function and integrity is not clear.

In this study, we probed the relationship between the status of cholinergic input to the EC and EC cognitive ability *in vivo* in healthy, older human volunteers. In healthy aging mice, we evaluated the integrity of cholinergic inputs to the EC and involvement of this circuit in EC-related object location memory. We compared these findings to those from a mouse model with genetic susceptibility to accumulation of amyloid and tau pathology. Our findings demonstrate that in both humans and mice, compromised cholinergic input to the EC occurs early in the aging process and is predictive of decreased cognitive performance on tasks that require the EC. Expression of familial AD-related genes and associated AD pathology accelerates the



time course of impaired EC cholinergic integrity. We find that deterioration of EC cholinergic circuits is an early and shared mechanism in natural and pathological aging.

## RESULTS

To gain better insight into the relationship between integrity of the cholinergic system and early cognitive impairment in both humans and mice we asked (1) whether alterations to the basal forebrain cholinergic system are an early feature of EC-related cognitive decline, and (2) what is the association between an intact cholinergic system and cognitive status?

### EC-related functions are diminished in older adults with cognitive impairment

To answer questions about the relationship between cholinergic system integrity and cognition, we recruited older adult volunteers (Table S1/Figure S1A) who were active in the community, physically healthy, devoid of comorbid mental health concerns, and without contraindications to positron emission tomography and magnetic resonance imaging (PET/MRI) scanning procedures. None of the volunteers had clinical diagnosis of cognitive impairment.

During the intake session we evaluated the cognitive status of each participant using the Montreal Cognitive Assessment (MoCA; Figure S1B, left), a sensitive clinical assessment for mild impairments in cognition.<sup>23</sup> Based on their intake-session MoCA score, participants were divided into two groups: older adults (OA, volunteers with intact cognition) and impaired older adults (OA-I, individuals with mild cognitive impairments) (Figure S1B, right). All participants also underwent the Penn Computerized Neurocognitive Battery (PennCNB), designed to assess cognitive status across multiple functional domains.<sup>24</sup> PennCNB performance was used to assess cognitive function between groups.

We first asked whether EC-related cognitive functions were altered in OA-I participants. Given the importance of the EC to object location memory,<sup>21,25,26</sup> we used the spatial visual object learning task (SVOLT and SVOLT-delayed) within the PennCNB to assess EC function in our participants. SVOLT evaluates memory performance in recognition of complex figures. During the SVOLT observation period, participants are presented with and asked to remember a series of three-dimensional shapes with shaded subregions (Figure 1A, left). During the test sessions (immediate vs. delayed), objects from the learning set were intermingled with new objects with different-shaded regions. For each presented object, participants were asked to recall whether the object was the same or different than what was presented during the observation session. The delayed test (SVOLT-D) was assessed following a 15- to 20-min delay during which time participants performed other cognitive tasks. We quantified the number of correct responses during the immediate and delayed testing session for participants in each group (OA vs. OA-I; Figures 1A, S1C, and S1D). OA-I participants performed significantly worse on the SVOLT-D task than their age-matched OA counterparts (Figure 1A, right; OA vs. OA-I,  $p = 0.03$ ). In contrast, performance did not significantly differ between groups on the immediate SVOLT (Figure S1C; OA vs. OA-I,  $p = 0.79$ ). We found that OA-I participants had a significantly

greater change in performance on the immediate vs. delayed SVOLT task compared to OA individuals (Figure S1D; OA vs. OA-I,  $p = 0.005$ ).

### EC cholinergic density is lower in older adults with cognitive impairment and correlates with object location memory performance

Next, we asked whether OA-I participants displayed differences in the synaptic integrity of cholinergic inputs in the EC. We quantified the density of the vesicular acetylcholine transporter (VACHT) *in vivo* using [<sup>18</sup>F]VAT PET (Figure 1). [<sup>18</sup>F]VAT specifically and selectively binds to VACHT, allowing us to quantify the integrity of the cholinergic system *in vivo*.<sup>27–30</sup> Linear mixed models were fit with [<sup>18</sup>F]VAT regional distribution volume (proportional to density) as the model outcome with group (OA or OA-I) and sex (male or female) as fixed effects, age as a covariate, and hemisphere (right and left) accounted for as a within-subject repeated measure. We found a significant main effect of group (and no main effect of sex), where EC distribution volumes were lower in OA-I participants compared to OA participants (Figures 1B and 1C,  $p = 0.046$ ). In contrast, distribution volumes in other areas (fit in individual models) such as the hippocampus (Figures 1E and 1F,  $p = 0.22$ ) or the somatosensory cortex (Figures 1H and 1I,  $p = 0.09$ ) did not differ.

To directly compare the relationship between cholinergic system integrity and SVOLT performance, we fit a model with SVOLT-D performance as the outcome and EC distribution volume as a fixed effect (covaried by hemisphere) for each group individually. Using an analysis of covariance (ANCOVA) test, we evaluated whether there was a difference in the relationship between cholinergic integrity and EC function (regression fits) between OA and OA-I groups (Figure 1D, black line vs. magenta line). We found a significant difference in the relationship between EC distribution volume and SVOLT-D task between groups (between-group effect of slopes,  $p = 0.001$ ), where participant performance significantly scaled to distribution volume in the OA-I but not OA groups. We performed the same ANCOVA test of regression fits for the hippocampus and somatosensory cortex and found no between-group differences in the regression fits in either region (Figure 1G, hippocampus,  $p = 0.12$ ; Figure 1J, somatosensory cortex,  $p = 0.16$ ).

### MS/vDB (CH1/2) VACHT density is lower in older adults with cognitive impairment

In rodents and non-human primates, cholinergic neurons in the medial septum/vertical limb of the diagonal band (MS/vDB) region innervate the EC, the hippocampal subfields, and the prefrontal cortex.<sup>3,31,32</sup> Using a previously validated BFCN subregion atlas,<sup>33</sup> we evaluated MS/vDB (CH1/2 in the BFCN subregion atlas), horizontal limb of the diagonal band (hDB; CH3 in the BFCN subregion atlas), and nucleus basalis/substantia innominata (nBM/SI; CH4p in the BFCN subregion atlas) distribution volumes across our groups (Figures 2 and S2). Linear mixed models were fit with MS/vDB distribution volume (proportional to density) as the model outcome with group (OA or OA-I) and sex (male or female) as fixed effects, age as a covariate, and hemisphere (right and left) accounted for as a within-subject repeated measure. We found that MS/vDB distribution volume

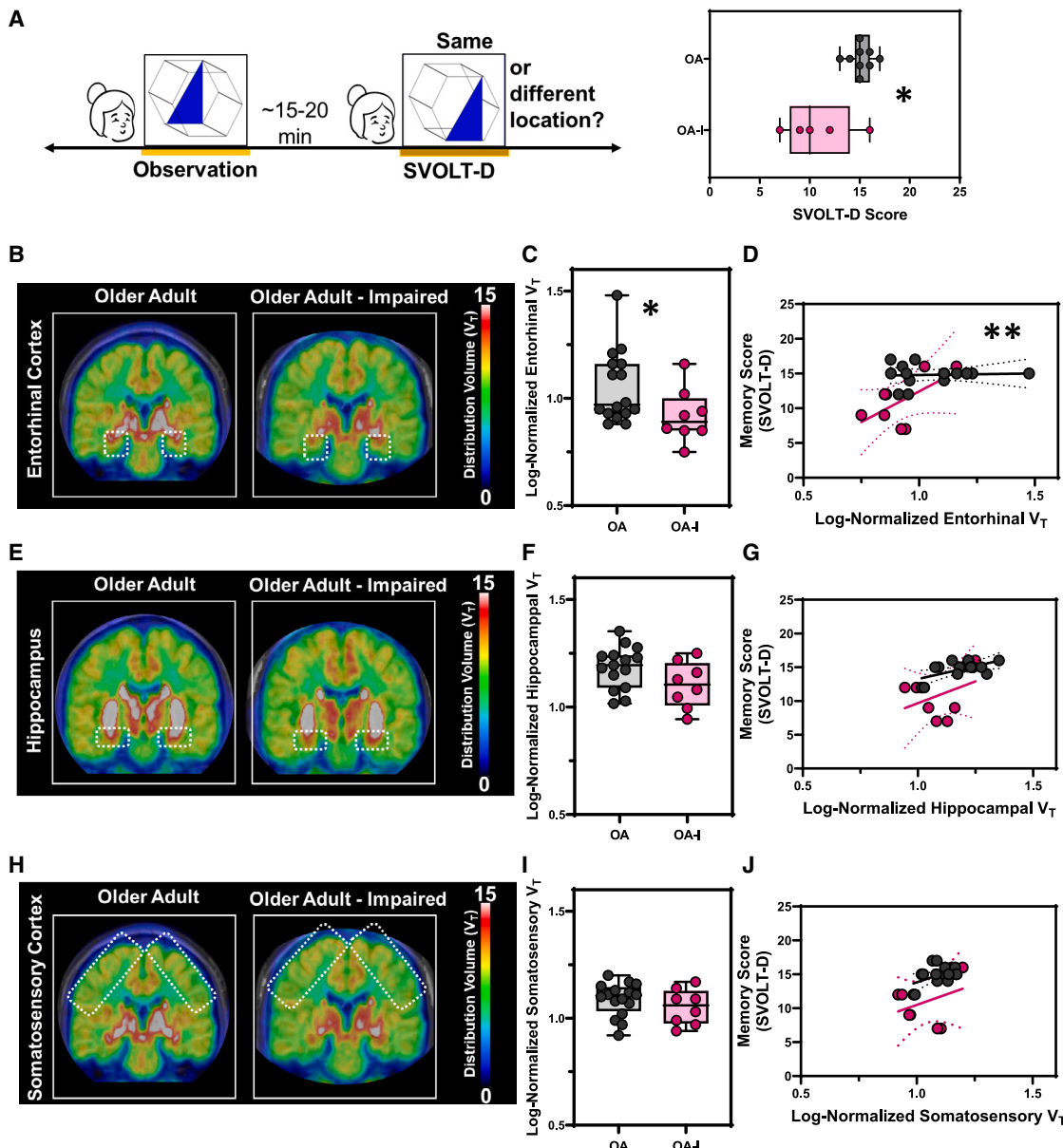


**Figure 1. EC VAT density is lower in older adults with cognitive impairment**

(A) (Left) Experimental workflow highlighting the object location learning task within the Penn computerized neurocognitive battery administered during the intake session. (Right) Delayed-spatial visual object learning task (SVOLT-D) between OA and OA-I participants.

(B, E, and H) Averaged maps of VACht density at each voxel from (left) older adults ( $n = 8$ ) vs. (right) impaired older adults ( $n = 4$ ) at the level of the (B) entorhinal cortex, (E) hippocampal formation, and (H) somatosensory cortex. Color bar represents distribution volume ( $V_T$ ).

(C, F, and I) Log-normalized right and left hemisphere  $V_T$  between older adults (OA,  $n = 8$ ) and impaired older adults (OA-I,  $n = 4$ ) in the (C) entorhinal cortex, (F) hippocampal formation, and (I) somatosensory cortex. Box plots summarize the median, upper, and lower quartiles. Errors bars denote range of data. Hemispheres plotted individually.

(D, G, and J) Correlation with linear regression (black or magenta line) comparing the relationship between [ $^{18}\text{F}$ ]VAT distribution volume and delayed memory score (SVOLT-D) in older adults and impaired older adults in (D) entorhinal cortex (comparison of regressions across groups), (G) hippocampal formation (comparison of regressions across groups), and (J) somatosensory cortex (comparison of regressions across groups). Hemispheres plotted individually. Linear regression distribution is colored gray for older adults and magenta for impaired older adults. See also Figures S1–S3 and Tables S1, S2, and S3.

was significantly lower in OA-I participants compared to OA participants (Figures 2A and 2B, main effect of group,  $p = 0.023$ ) with no main effect of sex. This group difference was not observed in

individually fit models evaluating group comparisons for nBM/SI (Figures 2D and 2E,  $p = 0.07$ ) or hDB (Figure S2A,  $p = 0.22$ ) distribution volumes.

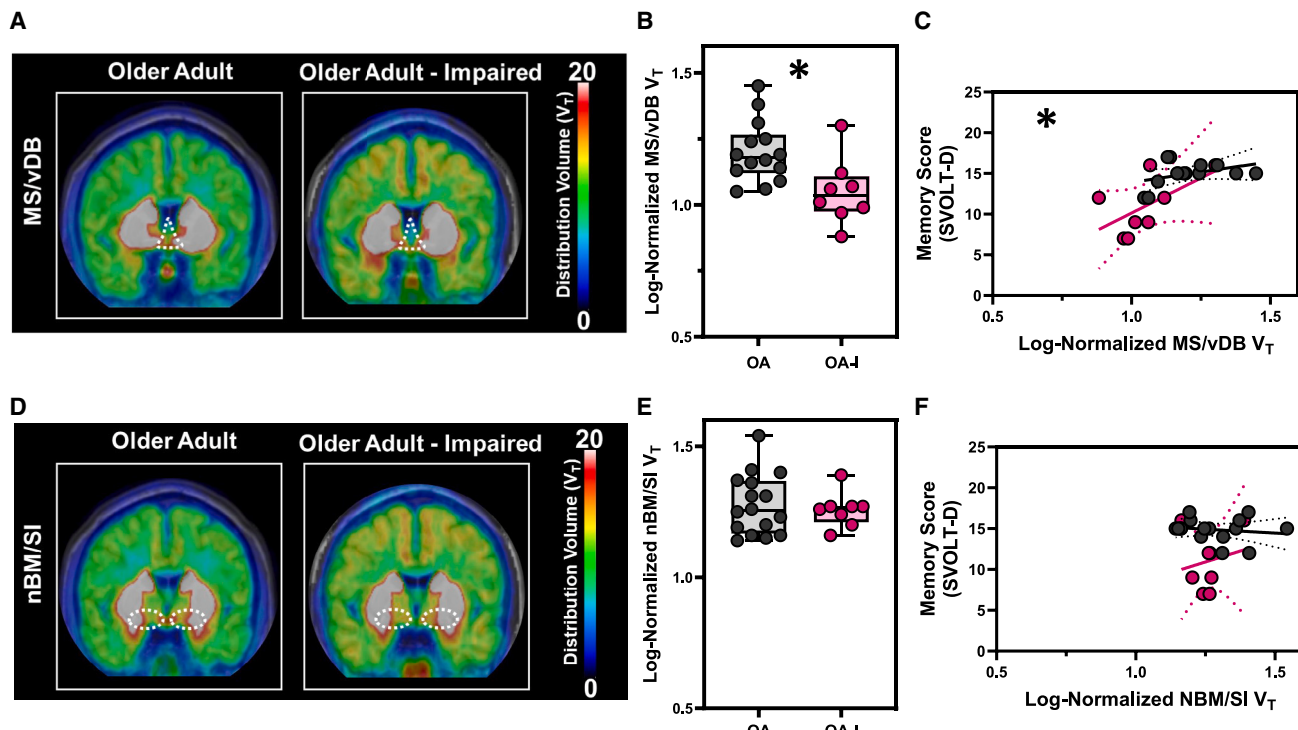


**Figure 2. MS/vDB VAT density is lower in older adults with cognitive impairment**

(A and D) Averaged maps of VACt density at each voxel from (left) older adults ( $n = 8$ ) vs. (right) impaired, older adults ( $n = 8$ ) at the level of the (A) medial septum/diagonal band (MS/vDB; CH1/CH2) and (D) nucleus basalis/substantia innominata (NBM/SI; CH4p). Color bar represents distribution volume ( $V_T$ ). (B and E) Log-normalized right and left hemisphere  $V_T$  between older adults (OA,  $n = 8$ ) and impaired older adults (OA-I,  $n = 4$ ) in the (B) MS/vDB and (E) NBM/SI. Box plots summarize the median, upper, and lower quartiles. Errors bars denote range of data. Hemispheres plotted individually. (C and F) Correlation with linear regression (black or magenta line) comparing the relationship between [ $^{18}\text{F}$ ]VAT distribution volume and delayed memory score (SVOLT-D) in older adults and impaired older adults in (C) MS/vDB (comparison of regressions across groups) and (F) NBM/SI (comparison of regressions across groups). Hemispheres plotted individually.

Linear regression distribution is colored gray for older adults and magenta for impaired older adults. See also Figures S1–S3 and Tables S1, S2, and S3.

To directly compare the relationship between cholinergic integrity in BFCNs and SVOLT performance, we fit a model with SVOLT-D performance as the outcome and MS/vDB distribution volume as a fixed effect for each group individually (covaried by hemisphere). Using an ANCOVA, we evaluated whether there was a difference in the relationship between MS/vDB distribution volumes and SVOLT-D performance between groups (Figure 2C, black line vs. magenta line). We found a significant difference in the regression slopes between groups such that larger MS/vDB distribution volumes corresponded with higher performance on the SVOLT-D in OA-I but not OA participants (Figure 2C, between-group effect of slopes,  $p = 0.009$ ). In contrast, there were no between-group differences in the regression fits in the nBM (Figure 2F,  $p = 0.11$ ) or hDB (Figure S2B,  $p = 0.27$ ).

#### The circuit between the MS/vDB and EC is structurally impaired in older adults with minor cognitive impairments

We found that OA-I participants had lower distribution volumes in both the MS/vDB (Figure 2) and the EC (Figure 1) that correlated with poor SVOLT-D performance. Given this, we next

asked whether there were deficits in the structural connectivity between the MS/vDB and EC in OA-I participants compared to their OA counterparts. Using diffusion-weighted MRI acquired simultaneously with the PET imaging, we reconstructed structural tracts between the MS/vDB (set as the seed region) and the EC (set as the region of interest [ROI]/end region) (Figure S3A). We quantified diffusion metrics along the rendered tract (Figure S3A, right) between the MS/vDB and the EC in each participant. We found reductions in fractional anisotropy (FA; Figure S3B [left],  $p = 0.01$ ) and elevations in both mean diffusivity (MD; Figure S3B [middle],  $p = 0.05$ ) and axial diffusivity (AD; Figure S3B [right],  $p = 0.05$ ) in OA-I participants compared to OA counterparts. These data are consistent with disordered, fragmented, and structurally impaired tracts between the MS/vDB and EC in human participants with minor impairments in EC cognition.

#### The displaced object recognition behavioral task activates the lateral EC in mice

The data presented above reveal a statistically significant relationship between EC-related memory performance and the integrity of the MS/vDB cholinergic projection to the EC in human

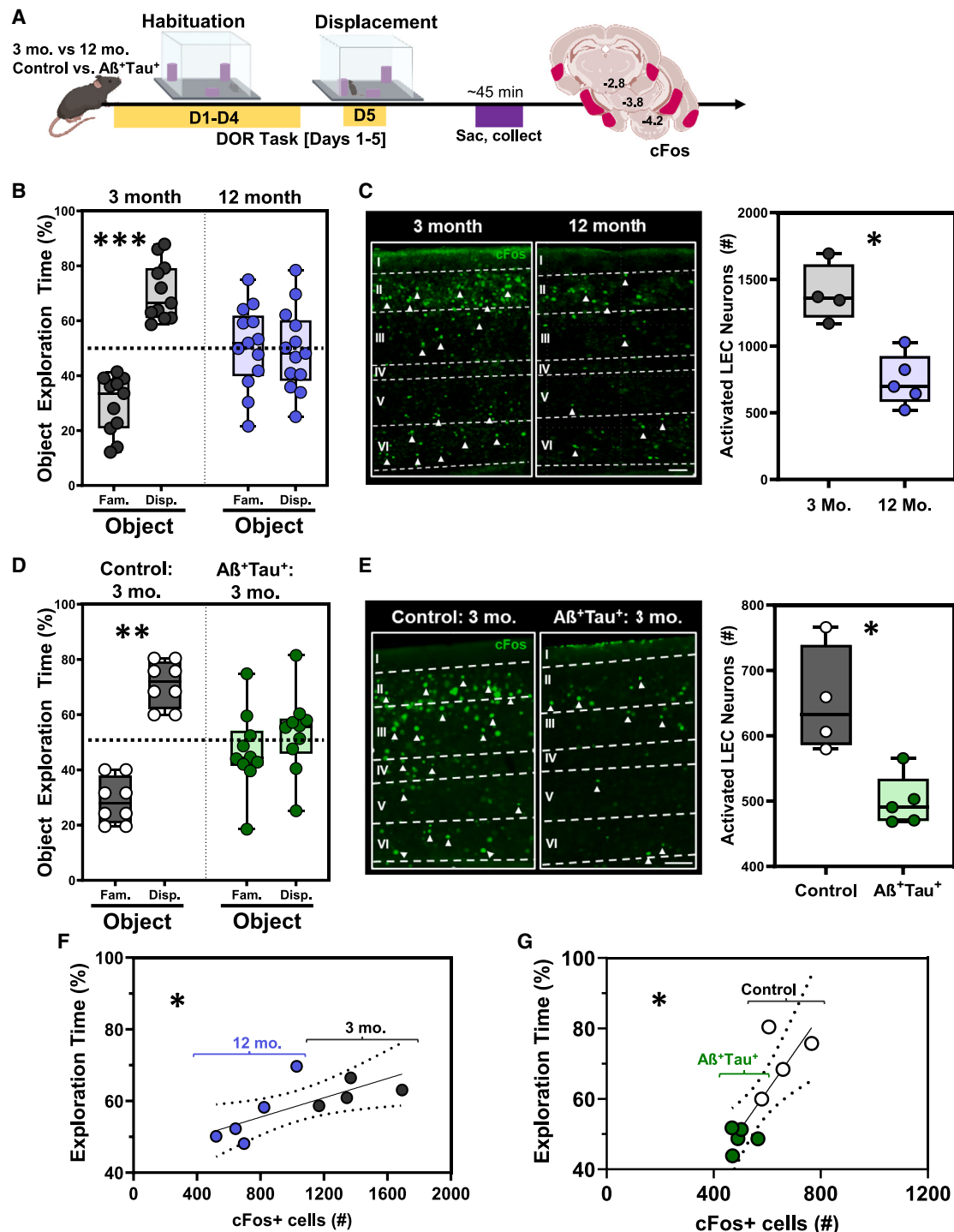


**Figure 3. LEC activation and DOR performance is lower in 12-month-old WT and  $\text{A}\beta^+\text{Tau}^+$  animals**

(A) Experimental workflow. WT or control/ $\text{A}\beta^+\text{Tau}^+$  animals were assessed in the displaced object recognition (DOR) task followed by tissue harvesting and cFos immunostaining.

(B) Quantification of percent time spent exploring familiar vs. displaced object during the displacement session in 3-month-old ( $n = 11$ ) and 12-month-old animals ( $n = 12$ ).

(C) (Left) Representative high-magnification images of LEC cFos activation during the displacement test in 3-month-old (left) vs. 12-month-old (right) animals; scale bar, 50  $\mu\text{m}$ . (Right) Quantification of total cFos activation in the EC during the displacement test in 3-month-old ( $n = 4$ ) vs. 12-month-old ( $n = 5$ ) animals.

(legend continued on next page)

subjects. To gain deeper insight into the function of acetylcholine in maintaining EC function, we turned to animal models. We focused our investigation on cholinergic circuits to the lateral entorhinal cortex (LEC, homologous to anterolateral entorhinal cortex [aLEC] in humans) given the LEC's early role in age-related vulnerabilities in humans.<sup>13,15,17,19-21</sup>

In rodents, the displaced object recognition (DOR) task closely mirrors the object location task administered in human studies. We first evaluated the potential of the DOR task to engage the mouse LEC. Mice were habituated to an environment with objects in set locations over four consecutive days (Figure S4A, habituation). On the test day, day 5, one object was displaced to a new location within the arena (Figure S4A, displacement). Typically, mice explore the newly displaced object more than they would the non-displaced objects, as illustrated in the sample heatmaps of "habituation" vs. "displacement" (Figure S4B) where object 3 was moved to a new location. Total object exploration time did not differ between habituation and displacement sessions (Figure S4C [left], black bars; male,  $p > 0.8$ ; female,  $p > 0.2$ ). During the displacement session, 3-month-old wild-type (WT) male and female mice spend more time exploring the displaced object (O3) compared to the identical familiar object (O1) (Figure S4C [left], displacement, O3 vs. O1 vs. O2; male,  $p = 0.004$ ; female,  $p = 0.004$ ). Exploration did not differ between objects during the habituation session. Subsequent analyses quantified percent of object exploration time spent exploring the familiar (O1) vs. displaced (O3) objects (Figure S4D,  $p = 0.0002$ ). Note that 3-month-old male and female WT mice displayed identical behavioral responses in this assay, even when expressed as percent time spent exploring (Figure S4C [right], Male Fam. vs. Disp.,  $p = 0.002$ ; Female Fam. vs. Disp.,  $p = 0.004$ ). In subsequent analyses, we collapsed sex as a biological variable and included both male and female mice in all experiments (e.g., Figure S4D).

To test for engagement of the LEC, we assessed immunoreactivity for expression of the immediate-early gene (IEG) product cFos 45 min following the DOR task (Figures S4E–S4G). Significantly more LEC neurons expressed cFos following the DOR session when compared to mice maintained in their home cages (HC; Figures S4F and S4G,  $p = 0.0001$ ). We also assessed cFos immunoreactivity in mice following habituation for five consecutive days (HAB), following a single session of object exploration (Novel Obj.), and following exploration of an empty arena for 5 days (OF) (Figures S4E and S4G) to better understand LEC involvement in object location memory. Consistent with the role of the EC in object encoding,<sup>21,25,26</sup> we found elevated cFos immunoreactivity in the habituation and novel object groups compared to the open-field and home-cage control conditions (Figure S4G, HC/OF vs. Novel Obj./HAB,  $p < 0.0005$ ).

DOR significantly elevated cFos in the LEC compared to novel object and habituation conditions (Figure S4G, Novel Obj./HAB vs. DOR,  $p < 0.001$ ) and open-field and home-cage conditions (Figures S4F and S4G, HC/OF vs. DOR,  $p < 0.0001$ ).

### Two distinct mouse models allow for evaluation of age and AD pathology on cholinergic integrity and LEC function

The DOR task provides a quantifiable measure of behavioral performance and engagement of the LEC.<sup>25,26</sup> To answer questions about the relationship between cholinergic system integrity and LEC function, we evaluated two mouse models. (1) To answer questions about the relationship between cholinergic system integrity and LEC function with age, we evaluated 12-month-old (middle-aged in mouse lifespan) mice and quantified their performance as compared to younger, 3-month-old mice. We specifically chose this time point to identify the earliest changes to the BFCN → EC circuit at a time that would be definitively considered "preclinical." (2) To answer questions about the relationship between cholinergic system integrity and LEC function that better mimic aspects of AD progression, we utilized A $\beta$ -over-expressing mice (5XFAD) combined with genetic deletion of NOS2. This cross (5XFAD × NOS2 $^{-/-}$ ) resulted in a new model that displayed spontaneous generation of hyperphosphorylated mouse tau (Figure S5) reminiscent of findings with APPSwDI, 3xFAD crossed with NOS2 $^{-/-}$ .<sup>34-36</sup> We compared A $\beta$  and hyperphosphorylated-tau accumulation in the LEC in a 5XFAD mouse line crossed to NOS2 $^{-/-}$  mice with that of all genetic controls (C57, NOS2 $^{-/-}$ , and 5XFAD) at 1.5, 3, 6, and 12 months of age (Figure S5). A $\beta$  plaques accumulated in 5XFAD $^{+/-}$  and 5XFAD × NOS2 $^{-/-}$  animals (Figure S5, A $\beta$  red plaques in third and fourth columns). No A $\beta$  accumulation was seen in WT or NOS2 $^{-/-}$  mice (Figure S5, first and second columns). Hyperphosphorylated tau was only detected in 5XFAD × NOS2 $^{-/-}$ , appearing by 3 months of age (Figure S5, pTau, green aggregates in fourth column vs. rest).

For subsequent experiments, 3-month-old 5XFAD × NOS2 $^{-/-}$  (Figure S5, A $\beta$  $^{+/-}$ Tau $^{+/-}$ : fourth column) were compared to NOS2 $^{-/-}$  littermate controls (Figure S5, littermate controls: second column) and 3-month-old WT mice (Figure S5, first column, second row) were compared to 12-month-old WT mice (Figure S5, first column, fourth row).

### Twelve-month-old WT and A $\beta$ $^{+/-}$ Tau $^{+/-}$ mice have impaired DOR performance and impaired activation of the LEC

To answer questions about the relationship between cholinergic system integrity and LEC function with age, we first evaluated EC function in 12-month-old (vs. 3-month-old) mice using the DOR task (Figure 3A). Object exploration was equivalent

(D) Quantification of percent time spent exploring familiar vs. displaced object during the displacement session between control ( $n = 8$ ) and A $\beta$  $^{+/-}$ Tau $^{+/-}$  animals ( $n = 10$ ).

(E) (Left) Representative high-magnification images of LEC cFos activation during the displacement session in control (left) vs. A $\beta$  $^{+/-}$ Tau $^{+/-}$  (right) animals. scale bar, 50  $\mu$ m. (Right) Quantification of total cFos activation in the EC during the displacement test in control ( $n = 4$ ) vs. A $\beta$  $^{+/-}$ Tau $^{+/-}$  ( $n = 5$ ) animals.

(F) Correlation plot with linear regression comparing the relationship between EC cFos activation (cFos $^{+/-}$ ) and DOR performance in 3-month-old vs. 12-month-old animals.

(G) Correlation plot with linear regression comparing the relationship between EC cFos activation (cFos $^{+/-}$ ) and DOR performance in control vs. A $\beta$  $^{+/-}$ Tau $^{+/-}$  animals. Box plots summarize the median, upper, and lower quartiles. Errors bars denote range of data. See also Figures S4–S6, S10, and Table S3.

between 3- and 12-month-old mice during the habituation session (**Figures S6A** and **S6B**; 3-month,  $p = 0.85$ ; 12-month,  $p = 0.29$ ). During the displacement session, 3-month-old mice spent more time exploring the displaced object (**Figure 3B**, gray bars,  $p = 0.001$ ), whereas 12-month-old mice spent equal time in the exploration of both the displaced and familiar objects (**Figure 3B**, purple bars,  $p = 0.69$ ). No differences were seen across sex within either the 3-month-old or 12-month-old mice (data not shown). To test whether altered performance was related to impaired activation of the LEC, we assessed cFos immunoreactivity following the DOR task. Mice were sacrificed 45 min following the test session and processed for expression of IE6 cFos (**Figure 3A**). Twelve-month-old animals had fewer activated neurons in the LEC following DOR than 3-month-old animals (**Figure 3C**,  $p = 0.02$ ).

We next quantified performance of  $\text{A}\beta^+\text{Tau}^+$  mice and littermate controls in the DOR task (**Figure 3A**). As expected, exploration of objects was equivalent between groups during the habituation session (**Figure S6A** and **S6C**; control,  $p = 0.69$ ;  $\text{A}\beta^+\text{Tau}^+$ ,  $p > 0.99$ ). During the displacement session, littermate controls spent more time exploring the displaced object (**Figure 3D**; gray bars,  $p = 0.002$ ), whereas  $\text{A}\beta^+\text{Tau}^+$  animals spent about equal time exploring both the displaced and familiar objects (**Figure 3D**; green bars,  $p = 0.22$ ). To test whether this altered performance was related to impaired activation of the LEC, we assessed cFos immunoreactivity following the DOR task (**Figure 3A**).  $\text{A}\beta^+\text{Tau}^+$  animals had fewer activated neurons, as reflected by fewer cFos<sup>+</sup> cells in the LEC, following DOR than littermate controls (**Figure 3E**,  $p = 0.02$ ).

We evaluated the relationship between activation of the LEC and performance on the DOR task in both mouse models. We found a significant relationship between engagement of the LEC and object location memory in WT mice (**Figure 3F**,  $r_S = 0.52$ ,  $p = 0.03$ ) as well as the control/ $\text{A}\beta^+\text{Tau}^+$  mouse model (**Figure 3G**,  $r_S = 0.73$ ,  $p = 0.03$ ). Overall, performance on the DOR task across groups directly correlated with cFos activation in the LEC.

### EC terminal field density is lower in 12-month-old WT and $\text{A}\beta^+\text{Tau}^+$ mice

Given the deficits in EC-related DOR performance and engagement of the EC, we asked whether there were changes in the integrity of cholinergic inputs in the LEC in either 12-month-old or  $\text{A}\beta^+\text{Tau}^+$  mice.

We used ChAT-tau:eGFP mice to evaluate cholinergic terminal field density in the LEC (**Figures 4A**, **4C**, **S7A–S7C**, and **S8**). In this strain, all cholinergic neurons and processes are labeled with a green fluorescent protein (GFP), allowing for whole-brain evaluation of cholinergic system integrity. We found that 12-month-old mice had significantly lower cholinergic terminal field density in the LEC than 3-month-old mice (**Figures 4B** and **4C**,  $p = 0.0002$ ). In contrast, cholinergic terminal density of 12-month-old mice in other cortical areas such as the somatosensory cortex did not significantly differ from 3-month-old mice (**Figures S7B** and **S7C**,  $p = 0.85$ ). We did not find differences in cholinergic terminal density of the EC in the developmental period between 1.5 months and 3 months of age (**Figures S8A** and **S8C**,  $p = 0.54$ ). VACHT density offers a comple-

mentary set of information to ChAT-tau:eGFP density, so we additionally compared VACHT immunoreactivity in the LEC between 12- and 3-month-old animals (**Figures S8B** and **S8D**), offering a direct comparison to [<sup>18</sup>F]VAT distribution volumes in humans. Consistent with our results, we found that VACHT density was also significantly lower in 12-month-old mice compared to 3-month-old mice (**Figures S8B** and **S8D**,  $p = 0.008$ ). These results parallel our findings with the tau:eGFP experiments and our observations using [<sup>18</sup>F]VAT PET in OA vs. OA-I participants.

We next asked whether there were changes in the integrity of cholinergic inputs in the LEC in  $\text{A}\beta^+\text{Tau}^+$  mice. We crossed  $\text{A}\beta^+\text{Tau}^+$  to ChAT-tau:eGFP mice and evaluated cholinergic terminal field density in the LEC (**Figures 4A**, **4D**, **4E**, **S7A**, **S7D**, **S7E**, and **S9**). We found that  $\text{A}\beta^+\text{Tau}^+$  animals had significantly lower cholinergic terminal field density in the LEC at 3 months compared to littermate controls (**Figures 4D** and **4E**,  $p < 0.0003$ ). In contrast, cholinergic terminal field density in other cortical areas such as the somatosensory cortex did not significantly differ between groups (**Figures S7D** and **S7E**,  $p = 0.98$ ). We found that cholinergic terminal field density in  $\text{A}\beta^+\text{Tau}^+$  mice did not differ from littermate controls at 1.5 months (**Figures S9A** and **S9C**, left column,  $p = 0.55$ ) but did differ by 3 months (**Figures 4D** and **4E**; **Figures S9A** and **S9C**, right column,  $p < 0.008$ ). These differences persisted through 12 months (**Figures S9A** and **S9C**, right column,  $p = 0.008$ ). We additionally compared VACHT immunoreactivity in the LEC between  $\text{A}\beta^+\text{Tau}^+$  and littermate controls (**Figures S9B** and **S9D**). We found that VACHT density was significantly lower in 3-month-old  $\text{A}\beta^+\text{Tau}^+$  mice compared to littermate controls (**Figures S9B** and **S9D**,  $p = 0.03$ ).

We evaluated the relationship between cholinergic system integrity and DOR performance in both mouse models. We found that greater cholinergic input in the EC correlated with better performance on the DOR task in the EC of WT (**Figure 4F**,  $r_S = 0.90$ ,  $p < 0.001$ ) and control/ $\text{A}\beta^+\text{Tau}^+$  (**Figure 4G**,  $r_S = 0.64$ ,  $p = 0.05$ ) mice. In contrast, we found no correlation between somatosensory cortex cholinergic terminal field density and DOR performance in either group (**Figure S7F**, WT mice,  $r_S = 0.0007$ ,  $p = 0.94$ ) (**Figure S7G**, control/ $\text{A}\beta^+\text{Tau}^+$  mice,  $r_S = 0.15$ ,  $p = 0.69$ ).

### Baseline EC activity is elevated in $\text{A}\beta^+\text{Tau}^+$ mice

$\text{A}\beta^+\text{Tau}^+$  mice displayed poor performance on the DOR task, blunted activation (as measured by cFos immunoreactivity) of the LEC following DOR, and lower cholinergic input to the LEC. To test whether these changes were accompanied by changes to LEC activity, we evaluated cFos immunoreactivity in  $\text{A}\beta^+\text{Tau}^+$  animals and littermate controls under a home-cage condition (**Figures S10A** and **S10B**). We found a significant difference in the number of cFos<sup>+</sup> cells between the control and  $\text{A}\beta^+\text{Tau}^+$  animals (**Figure S10B**,  $p = 0.016$ ), where  $\text{A}\beta^+\text{Tau}^+$  animals had more activated neurons at baseline than their littermate control counterparts. When compared to cFos activation following DOR (**Figure S10C** vs. **Figure S4G**), we found control animals displayed a ~60% increase in cFos<sup>+</sup> immunoreactivity in the LEC from home cage to DOR, while  $\text{A}\beta^+\text{Tau}^+$  animals displayed only an ~10% increase in cFos. Given the elevated activation of the LEC at baseline conditions and the modest change in cFos<sup>+</sup> activation following DOR in the  $\text{A}\beta^+\text{Tau}^+$  animals, we hypothesized  $\text{A}\beta^+$

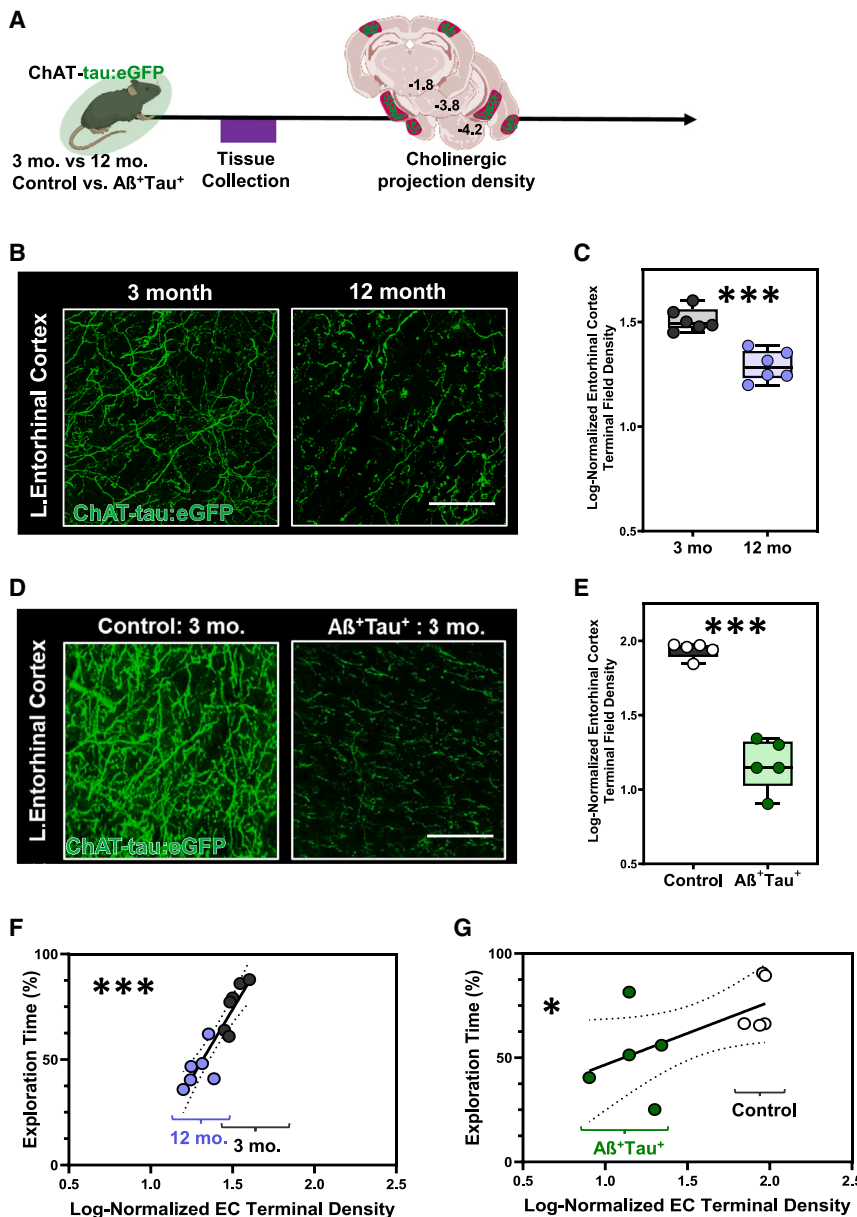


**Figure 4. LEC cholinergic terminal density is lower in 12-month-old WT and A $\beta$ +Tau $^+$  animals**

(A) Experimental workflow. WT, control, and A $\beta$ +Tau $^+$  animals were crossed to the ChAT-tau:eGFP line and evaluated for cholinergic terminal field integrity.

(B and D) High-magnification representative confocal images of entorhinal cortex (EC) in (B) 3-month-old (left) vs. 12-month-old (right) animals and (D) control (left) vs. A $\beta$ +Tau $^+$  (right) animals. Scale bars, 50  $\mu$ m.

(C and E) Quantification of cholinergic terminal field density in EC in (C) 3-month (n = 6) vs. 12 month (n = 5) mice and (E) control (n = 5) vs. A $\beta$ +Tau $^+$  (n = 5) mice.

(F and G) Correlation plots with linear regression line comparing the relationship between cholinergic terminal field density and DOR performance in the EC in (F) 3-month vs. 12-month WT mice and (G) control vs. A $\beta$ +Tau $^+$  mice.

Box plots summarize the median, upper, and lower quartiles. Error bars denote range of data. See also Figures S4, S5, S7–S10, and Table S3.

cognitive decline in our two mouse models. To evaluate whether changes to EC-projecting cholinergic neurons contributed to dysfunction in this circuit, we first mapped the origin of cholinergic input to the LEC using a retrograde tracer, Fast Blue, delivered directly into the LEC of 3-month-old ChAT-tau:eGFP mice<sup>37</sup> (Figure S11A, left). We found back-labeled cholinergic neurons (i.e., neurons that were both Fast Blue $^+$  and ChAT $^+$ ) primarily in the MS and vDB, with the remainder in the hDB. No back-labeled cells were found in the nBM. Back-labeled cells represented about 10% of MS/vDB cholinergic neurons (Figure S11A, right).

Next, to determine whether MS/vDB cholinergic neurons participate in object encoding during the DOR task, we evaluated cFos immunoreactivity in the MS/vDB of 3-month-old WT mice after DOR testing (Figure S11B). Mice were sacrificed 45 min after behavior and were compared to animals that never left their home cage (Figure S11C). We found that the total number of activated (cFos $^+$ ) cholinergic neurons in the MS/vDB following the displacement test (Figure S11C/D) was significantly greater compared to home cage controls ( $p = 0.01$ ).

#### MS/vDB cholinergic neurons are functionally impaired in 12-month-old WT and A $\beta$ +Tau $^+$ mice

By 12 months of age, in otherwise healthy mice we observe specific changes in the MS/vDB → EC circuit including lower DOR performance, lower cholinergic input to the EC, and impaired engagement of the EC following the DOR task. To test whether

Tau $^+$  may display hyperactivity in the LEC at baseline. To test this, we used anesthetized *in vivo* recordings to evaluate the baseline LEC activity in A $\beta$ +Tau $^+$  mice and littermate controls (Figure S10C–S10E). Electrodes were placed in the LEC, and single-unit baseline activity was recorded. We found that LEC recordings from A $\beta$ +Tau $^+$  mice displayed elevated firing rate, with a highly disorganized firing pattern, when compared to control animals (Figures S10D and S10E,  $p = 0.034$ ), consistent with hyperactivity of the LEC.

#### MS/vDB cholinergic neurons project to the LEC and are activated by the DOR behavioral task

We observed substantial changes to cholinergic integrity of the LEC and corresponding changes to LEC performance early in

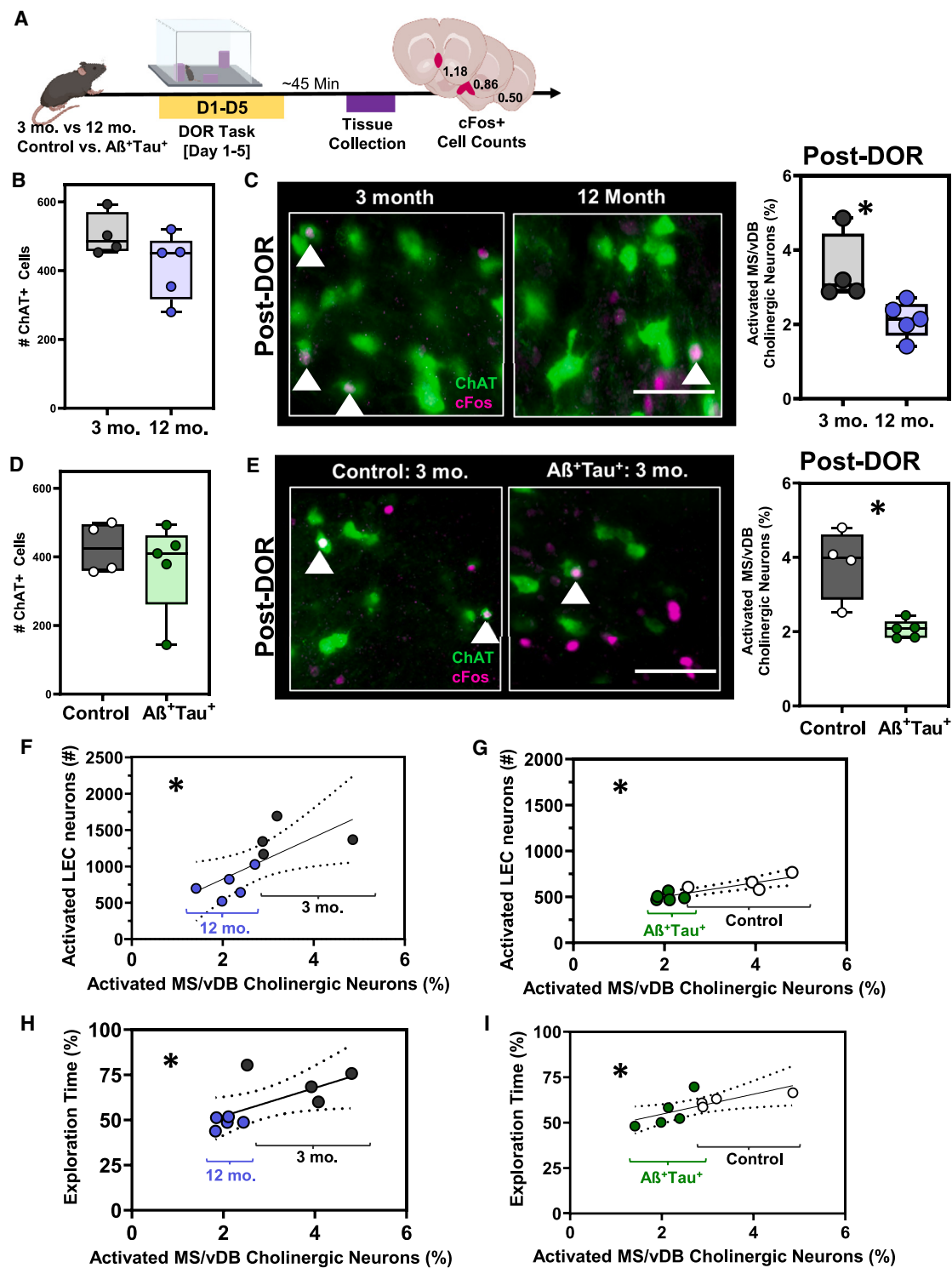


**Figure 5. Activation of MS/vDB cholinergic neurons is lower in 12-month-old WT and A $\beta^+$ Tau<sup>+</sup> animals and correlates with lower LEC activation and poorer DOR performance**

(A) Experimental workflow. WT or control/A $\beta^+$ Tau<sup>+</sup> animals were put through the displaced object recognition (DOR) task followed by tissue harvesting and cFos immunostaining.

(legend continued on next page)

these changes correspond with functional changes to cholinergic neurons, we evaluated cFos expression in MS/vDB cholinergic neurons after the DOR task (Figure 5A). Although there was no significant difference in the total number of cholinergic (ChAT<sup>+</sup>) neurons in the MS/vDB in 3-month-old vs. 12-month-old mice (Figure 5B,  $p = 0.19$ ), 12-month-old animals displayed fewer activated cholinergic neurons following DOR than 3-month-old animals (Figure 5C,  $p = 0.02$ ). We also evaluated cFos activation of MS/vDB cholinergic neurons in the A $\beta^+$ Tau<sup>+</sup> mice after DOR performance (Figure 5A). Although we found no differences in the total number of MS/vDB ChAT<sup>+</sup> neurons in control vs. A $\beta^+$ Tau<sup>+</sup> mice (Figure 5D,  $p = 0.90$ ), the A $\beta^+$ Tau<sup>+</sup> mice had fewer activated (cFos<sup>+</sup>) cholinergic neurons following DOR than littermate controls (Figure 5E,  $p = 0.02$ ).

We compared the relationship between cFos activation of cholinergic neurons in MS/vDB and subsequent cFos activation of LEC neurons following DOR (Figures 5F and 5G). We found a significant positive correlation between MS/vDB cholinergic neuron activation and LEC activation, where more cFos<sup>+</sup> neurons in the MS/vDB correlated with more cFos<sup>+</sup> neurons in the LEC in WT mice (Figure 5F,  $r_S = 0.51$ ,  $p = 0.03$ ) and control/A $\beta^+$ Tau<sup>+</sup> mice (Figure 5G,  $r_S = 0.77$ ,  $p = 0.02$ ).

We also examined the relationship between cFos activation of the MS/vDB and DOR performance (Figure 5H) and found a significant positive correlation between cFos<sup>+</sup> cholinergic neurons in the MS/vDB and performance on the DOR task in WT mice (Figure 5H,  $r_S = 0.53$ ,  $p = 0.03$ ) and control/A $\beta^+$ Tau<sup>+</sup> mice (Figure 5I,  $r_S = 0.80$ ,  $p = 0.01$ ).

### LEC-projecting cholinergic neurons are necessary for proper DOR performance

Activation of cholinergic neurons was related to both activation of the LEC and subsequent DOR performance. To determine whether normal cholinergic signaling to LEC is required for normal DOR performance, we injected the LEC of 3-month-old ChAT-IRES-Cre-Δneo mice with CAV<sub>2</sub>-DIO-hM4Di.mCherry and an AAV<sub>9</sub>-hSyn-eGFP (DREADDi animals) or AAV<sub>9</sub>-hSyn-eGFP alone (control animals) (Figure 6A). DREADDi and control animals were administered clozapine intraperitoneally at concentrations sufficient for selective activation of the DREADDi 10 min prior to the object displacement test session (Figure 6A).

Tissue was processed for relocalization of the injection site and verification of mCherry<sup>+</sup> cells in the MS/vDB (Figure 6B). Clozapine injection had no effect on total object exploration time between groups ( $p > 0.99$ ). Clozapine injection had no significant effect on control animal behavior; animals spent more time exploring the displaced object than the familiar object (Figures 6C and 6D, gray bars,  $p = 0.0002$ ). Inhibition of MS/vDB cholinergic neurons resulted in less time exploring the displaced object compared to the familiar object (Figures 6C and 6D, purple bars,  $p = 0.008$ ). Thus, activity of EC-projecting cholinergic neurons is required for proper DOR performance.

### A model for cholinergic system deterioration

To better understand the time course of cholinergic system deterioration across the lifespan, we combined our normalized data across species. We computed a composite EC integrity score that considered the log-normalized cholinergic system integrity (VAT distribution volume or terminal field density) and EC function (performance on the SVOLT-D or DOR task). We plotted these data across performance, coded by group (healthy in black vs. impaired in magenta) (Figure 7A). Taken together, we found a significant linear distribution across our datasets (human and both mouse models) where overall EC integrity was strongly predictive of EC performance (Figure 7A, \*\*\*,  $r_S = 0.75$ ,  $p < 0.001$ ). We further divided these data into an evaluation of controls and (mildly) impaired (across species) and found strong associations between EC integrity and performance within each group (healthy control; Figure 7B, \*\*\*,  $r_S = 0.75$ ,  $p < 0.001$ ) (mild impairment; Figure 7C, \*\*\*,  $r_S = 0.83$ ,  $p < 0.001$ ). We find that deterioration of EC cholinergic circuits is an early and shared mechanism in natural and pathological aging across species.

### DISCUSSION

In this PET/MRI study of aging humans and parallel anatomical and functional experiments on healthy aging and genetically modified mice, we find that cholinergic input from the MS/vDB to the EC begins to deteriorate at early stages of even minor cognitive impairments in a mechanism that is shared across both normal and pathological aging. In both species, the decrease in cholinergic terminal field integrity in the EC

- (B) Quantification of number of ChAT<sup>+</sup> neurons in MS/vDB of 3-month-old ( $n = 4$ ) vs. 12-month-old ( $n = 5$ ) animals ( $p = 0.19$ ).
  - (C) (Left) Representative high-magnification images of MS/vDB cFos activation following the displacement session of the DOR task in 3-month-old (left) vs. 12-month-old (right) animals. Scale bar, 50  $\mu$ m. White arrows denote cFos<sup>+</sup> and ChAT<sup>+</sup> (activated cholinergic) neurons. (Right) Quantification of percent activated cholinergic neurons in the MS/vDB of 3-month-old ( $n = 4$ ) vs. 12-month-old ( $n = 5$ ) animals following the displacement session of the DOR task.
  - (D) Quantification of number of ChAT<sup>+</sup> neurons in MS/vDB of control ( $n = 4$ ) vs. A $\beta^+$ Tau<sup>+</sup> ( $n = 5$ ) animals.
  - (E) (Left) Representative high-magnification images of MS/vDB cFos activation following the displacement session of the DOR task in control (left) vs. A $\beta^+$ Tau<sup>+</sup> (right) animals. Scale bar, 50  $\mu$ m. White arrows denote cFos<sup>+</sup> and ChAT<sup>+</sup> (activated cholinergic) neurons. (Right) Quantification of percent activated cholinergic neurons in the MS/vDB of control ( $n = 4$ ) vs. A $\beta^+$ Tau<sup>+</sup> ( $n = 5$ ) animals following the displacement session of the DOR task.
  - (F) Correlation plot with linear regression line comparing the relationship between percent activated cholinergic neurons (ChAT<sup>+</sup> and cFos<sup>+</sup>) in the MS/vDB and LEC cFos activation (cFos<sup>+</sup>) following the displacement test in 3-month-old ( $n = 4$ ) and 12-month-old ( $n = 5$ ) animals.
  - (G) Correlation plot with linear regression line comparing the relationship between percent activated cholinergic neurons (ChAT<sup>+</sup> and cFos<sup>+</sup>) in the MS/vDB and LEC cFos activation (cFos<sup>+</sup>) following the displacement test in control ( $n = 5$ ) and A $\beta^+$ Tau<sup>+</sup> ( $n = 5$ ) animals.
  - (H) Correlation plot with linear regression comparing the relationship between percent activated cholinergic neurons (ChAT<sup>+</sup> and cFos<sup>+</sup>) in the MS/vDB following DOR displacement session and DOR performance in 3-month-old ( $n = 4$ ) vs. 12-month-old ( $n = 5$ ) animals.
  - (I) Correlation plot with linear regression comparing the relationship between the percent activated cholinergic neurons (ChAT<sup>+</sup> and cFos<sup>+</sup>) in the MS/vDB following DOR displacement session and DOR performance in control ( $n = 4$ ) vs. A $\beta^+$ Tau<sup>+</sup> ( $n = 5$ ) animals.
- Box plots summarize the median, upper, and lower quartiles. Errors bars denote range of data. See also Figure S11 and Table S3.

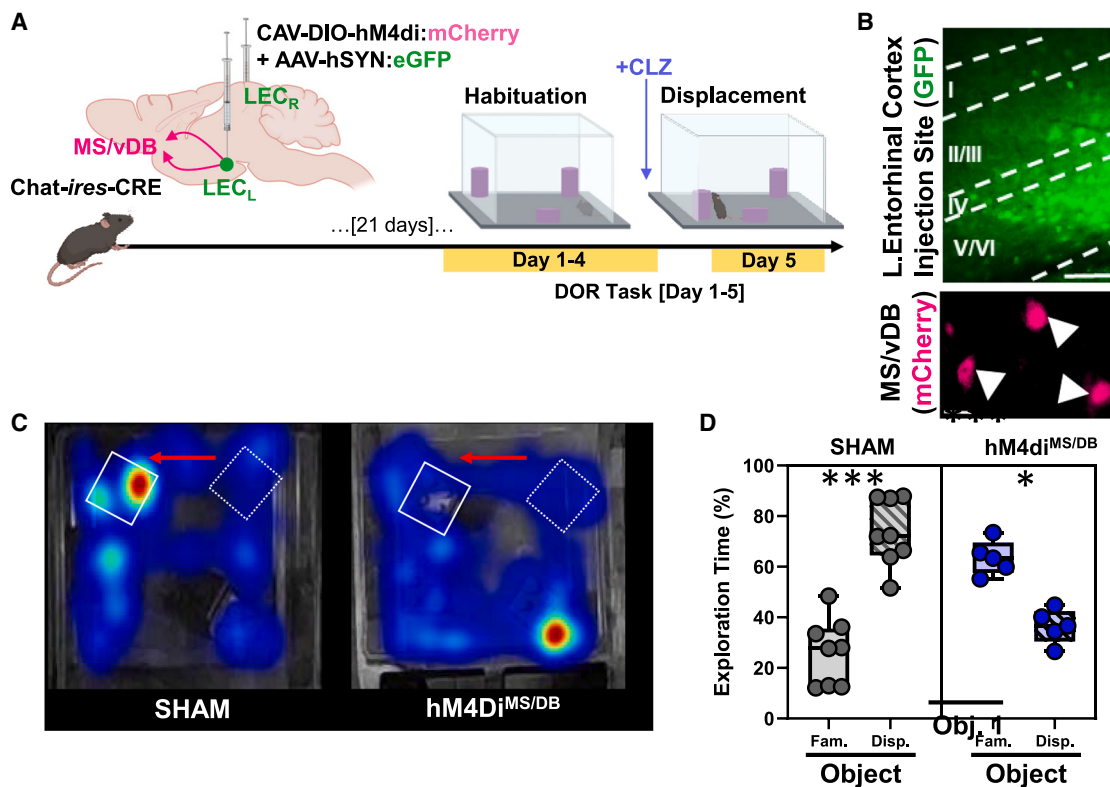


**Figure 6. Silencing LEC-projecting cholinergic neurons in young WT mice impairs DOR performance**

(A) Experimental workflow. Young, 3-month-old, Chat-cre animals were injected with a retrograde inhibitory DREADD construct (CAV-DIO-hM4di:mCherry) and a GFP control virus (AAV-hSYN:eGFP) to mark the injection site in LEC for cell-type-specific and projection-specific manipulation of cholinergic signaling (to the EC) during the displaced object recognition (DOR) task. Clozapine (0.1 mg/kg) was administered via intraperitoneal injection (to activate the DREADD) 10 min prior to the displacement session (day 5).

(B) (Top) Representative image of LEC injection site. Scale bar, 50  $\mu$ m. (Bottom) Representative image of hM4Di-expressing neurons in the MS/vDB, demonstrating successful, Cre-specific back-labeling of EC-projecting cholinergic neurons. Scale bar, 25  $\mu$ m.

(C) Representative heatmap showing arena exploration in control sham group (left) vs. hM4di<sup>MS/DB</sup> inhibition (right) group. Red arrows denote direction of displacement. Hot colors on the heatmap represent more time spent exploring, while cool colors represent less time spent exploring.

(D) Quantification of percent object exploration between the objects in control ( $n = 7$ ) vs. hM4di<sup>MS/DB</sup> ( $n = 5$ ) mice. Data indicate that the preference for the displaced object is blocked by inhibition of cholinergic projection neurons residing in the MS/vDB.

Box plots summarize the median, upper, and lower quartiles. Error bars denote range of data. See also Figure S4 and Table S3.

correlates with impaired performance on EC-related memory tasks. Selective manipulations of the cholinergic system in young mice are sufficient to impair object location memory, mimicking age-related disturbances to EC function. These data are consistent with a primary role of acetylcholine in the cognitive deficits associated with early EC dysfunction in age-related cognitive decline.

#### Loss of cholinergic input in the (lateral) EC is an early feature of cognitive decline

Postmortem studies report loss of cholinergic markers and neurons in individuals with AD.<sup>5–7</sup> Using recent advances in *in vivo* imaging methods,<sup>27–29</sup> we evaluated cholinergic synaptic integrity in the human EC, a region susceptible to aging and neurodegenerative disease. We find that loss of cholinergic input to the EC is an early occurrence in the progression of cognitive decline in otherwise healthy aging humans. Deterioration of cholinergic input to the EC is also apparent in “middle-aged” mice and

accelerated in animals that are genetically modified to express A $\beta$  and hyperphosphorylated tau.

It is well established that EC function is required for object location memory in primates and rodents.<sup>19,21,26,38–40</sup> Likewise, projection patterns of the basal forebrain cholinergic system are conserved across species.<sup>3,41,42</sup> Here we find that in addition to the anatomical connectivity and functional role of the EC, the function of the EC-projecting cholinergic circuit and the vulnerability of this circuit early in cognitive impairment are also conserved in human and mouse. As such, cross-species investigation of the mechanisms underlying cognitive impairment is of clinical relevance.

In mouse studies, we evaluated the vulnerability of the EC-projecting cholinergic circuit in both healthy aging animals and animals with genetic susceptibility to accelerated AD pathology. Even with the aggravated accumulation of AD pathology, the same cholinergic circuit is affected in a similar manner, underscoring the specific vulnerability of this circuit in normal and

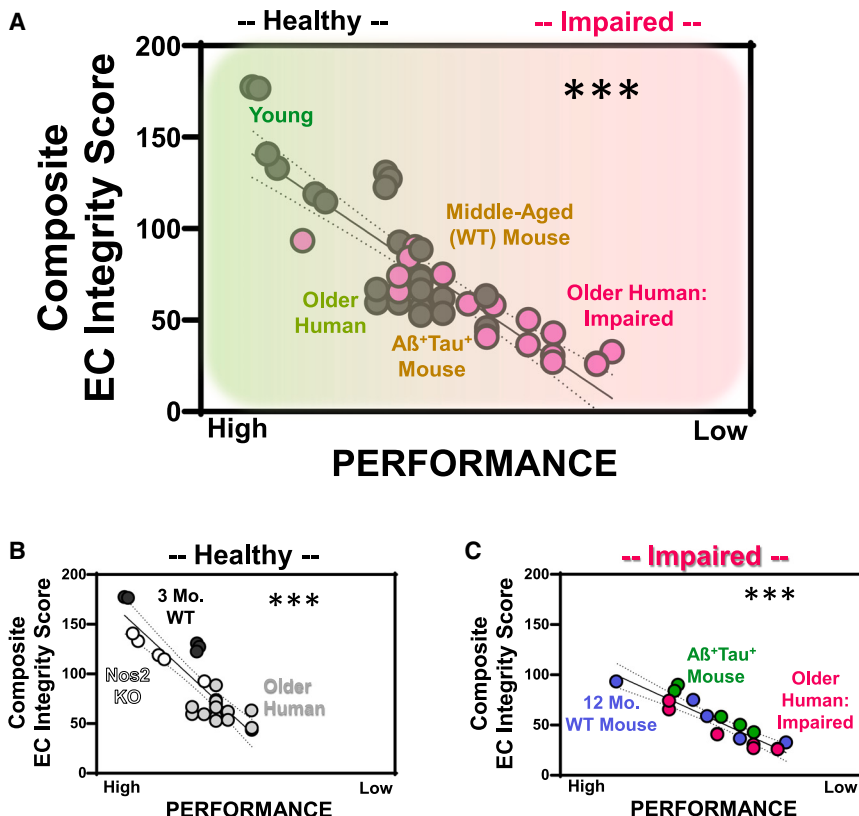


**Figure 7. Composite score for cholinergic terminal integrity and LEC performance from both mouse and human data**

(A) We computed composite scores using log-normalized cholinergic terminal integrity  $\times$  SVOLT-D performance (for human) and log-normalized cholinergic terminal integrity  $\times$  DOR performance (for mouse). Data were then coded to control (gray) or impaired (pink) groups and plotted against performance. Data were fit with a linear regression showing a strong correlation between performance and composite EC integrity. Text labels denote the group designation for clusters of points. Green to pink gradient denotes cholinergic terminal field integrity  $\times$  performance, with increasing pink indicating compromised.

(B) Composite EC integrity score for control data only.

(C) Composite EC integrity score for impaired data only.

See also Table S3.

The distribution of [ $^{18}\text{F}$ ]VAT accurately reports VACHT expression in the brain and can be used to measure cholinergic projections as well as cholinergic cell bodies.<sup>46</sup> We find that early in the progression of cognitive impairment, MS/vDB (CH1/2) cholinergic integrity (volume of distribution) is lower in OA-I participants.

Although our data are cross-sectional, this likely reflects changes in VACHT levels in cholinergic soma and/or local axons. We did not find decreased cholinergic integrity in HDB (CH3) or nBM/SI (CH4) nuclei.

Leveraging higher-resolution imaging capability in mice, we were able to use ChAT immunoreactivity to count MS/vDB cholinergic neurons and found no differences between 3-month-old and 12-month-old animals or control and cognitively impaired A $\beta$ +Tau+ mice. Although the overall numbers of MS/vDB cholinergic neurons did not differ, the functional engagement of MS/vDB cholinergic neurons by object location memory was significantly lower in mice with impaired DOR performance. This suggests that lower MS/vDB volume of distribution found in OA-I participants may reflect decreased VACHT expression due to loss of function of cholinergic neurons rather than a loss of cholinergic neurons per se.

A prior seed-to-searchlight MRI analysis found that basal forebrain nuclear degeneration covaries with cortical degeneration, reflective of their projections.<sup>47</sup> Our data are consistent with this hypothesis that the local EC cholinergic terminal integrity and the integrity of EC-projecting cholinergic circuits are among the earliest affected. Our targeted diffusion imaging analysis of the structural integrity of the circuit between the MS/vDB and the EC in humans was consistent with disordered, fragmented, and structurally impaired connectivity. Affected parameters included decreases in the anisotropic diffusion and increases in mean and axial diffusivity, consistent with a loss of white matter integrity as reported in neurodegenerative conditions<sup>48</sup> and advanced age.<sup>49</sup>

pathological aging, albeit at different rates. It is reasonable to assume that with further evaluation at later time points additional cholinergic regions and circuits could be affected in the genetically susceptible or aging WT animals that differ in onset and trajectory, reflective of the progression of normal to pathological aging. Yet it remains striking that the inherent vulnerability in the circuit encompassing the MS/vDB and the EC is conserved across these very different mechanisms of aging.

In human studies (when possible) we also evaluated the apolipoprotein E (*APOE*) genotype. The ApoE protein is critical in mediating lipid homeostasis and is thought to play a role in amyloid plaque aggregation and clearance in the brain.<sup>43,44</sup> Genome-wide association studies suggest that the  $\epsilon 4$  allele of the *APOE* gene is one of the strongest risk factors for dementia and AD as well as earlier age of onset.<sup>43,45</sup> In the present study, in evaluated samples, we find a higher occurrence of  $\epsilon 4$  heterozygotes in the OA-I group as compared to the OA group, consistent with the potential for elevated risk of cognitive impairment in  $\epsilon 4$  carriers. This population was recruited as otherwise healthy without a clinical diagnosis of cognitive impairment. Despite this, we are already able to identify loss of integrity of EC cholinergic input and EC-related cognitive deficits, highlighting the potential importance of the integrity of this circuit as an early diagnostic marker.

#### Functional changes in the basal forebrain projection to the EC precede cell loss

We evaluated the integrity of basal forebrain cholinergic nuclei in our human cohort using an established segmentation atlas.<sup>33</sup>

**Acetylcholine plays a critical role in EC function and performance**

The EC receives dense glutamatergic, GABAergic, and cholinergic input<sup>50</sup> from the medial septum and diagonal band nucleus. Cholinergic terminals in the LEC synapse onto both principal neurons and interneurons that express a variety of muscarinic and nicotinic acetylcholine receptors at both pre- and postsynaptic sites.<sup>51</sup> As a result, the net activity of acetylcholine in the LEC is complex and likely to be coordinated in a behaviorally relevant manner. In our mouse studies, we find that there are significant correlations between the extent of MS/vDB cholinergic activation, the integrity of their projections to the EC, and the activation of EC neurons and DOR performance. Perhaps most compelling, chemogenetic inhibition of EC projecting cholinergic neurons in healthy young mice disrupts DOR performance. Our results are consistent with the hypothesis that appropriate acetylcholine tone in the EC is important for proper EC function.

$\text{A}\beta^+\text{Tau}^+$  animals display elevated baseline and more disorganized firing activity compared to littermate controls. This finding of hyperexcitability in aging circuits is congruent with a growing body of literature.<sup>15,52,53</sup> There are several mechanisms that could underlie this phenotype: (1)  $\text{A}\beta$  accumulation could directly contribute to downstream synaptic dysfunction,<sup>54</sup> (2) loss of cholinergic input could result in imbalance of excitation/inhibition due to loss of cholinergic drive on inhibitory interneurons,<sup>55</sup> and (3) loss of input from the population of EC-projecting cholinergic neurons that coexpress/corelease GABA<sup>51</sup> could directly decrease GABAergic tone in the EC. Indeed, studies have found that boosting GABAergic tone in the EC can attenuate EC hyperactivity.<sup>52</sup> We propose that loss of EC cholinergic input results in elevation of circuit activity (increased baseline excitability) and an inability to specifically activate the EC in a behaviorally relevant manner (impaired cFos activation of MS/DB and EC), resulting in impaired object location memory performance. In support of this, silencing EC-projecting cholinergic input in normal animals is sufficient to dramatically affect object location memory performance.

**Quantifying vesicular acetylcholine transporter *in vivo* in humans using [<sup>18</sup>F]VAT**

Reliable quantification of cholinergic nuclei and terminal fields is possible using PET tracers that target the VACHT. Two such probes have recently been developed: [<sup>18</sup>F]FEOBV<sup>56</sup> and [<sup>18</sup>F]VAT.<sup>27</sup> FEOBV has been used in rodents,<sup>57,58</sup> nonhuman primates,<sup>58</sup> and healthy human volunteers.<sup>47,56,59–61</sup> Quantifying FEOBV is limited by slow kinetics that necessitate using either long scan times or short semi-quantitative static scans that rely on estimates of non-equilibrium tissue ratios including standardized uptake value ratios (SUVR). Tu et al.<sup>27</sup> generated [<sup>18</sup>F]VAT by modifying FEOBV's structure. Early studies in rodents<sup>27</sup> and non-human primates<sup>28,29</sup> demonstrate that VAT has the faster kinetics necessary for fully quantitative measurement of VACHT throughout the brain. Based on these findings, we chose to utilize [<sup>18</sup>F]VAT for *in vivo* PET imaging of cholinergic terminal field integrity in an elderly population of humans. Using metabolite-corrected arterial plasma [<sup>18</sup>F]VAT concentration as input, we estimated VACHT distribution volume in key regions of interest throughout the brain. We were able to demonstrate differen-

tial terminal field loss in EC vs. hippocampus and somatosensory cortex in subjects who showed cognitive deficits on both the MOCA and PennCNB SVOLT tests. Notably, these individuals were not recruited based on an existing clinical diagnosis but were part of a healthy community-based cohort. These results indicate that there are quantifiable losses in cholinergic terminal integrity in the EC in healthy individuals that correlate with reduced performance on cognitive tasks.

Previous studies evaluated cortical FEOBV SUVR in participants recruited with a diagnosis of mild cognitive impairment (MCI)<sup>60</sup> or AD.<sup>59</sup> These studies reported global deficits in cortical cholinergic innervation in individuals in the MCI or AD groups.<sup>60</sup> We evaluated a population without clinical diagnosis of cognitive impairment, albeit with subjective memory concerns. Our studies extend upon existing findings to assess the integrity of cholinergic circuitry early in cognitive impairment and probe the cholinergic mechanisms underlying impaired EC function.

It has previously been found that VACHT uptake was a better predictor of AD than either amyloid-beta load (<sup>[18]</sup>F)NAV uptake) or brain glucose metabolism (<sup>[18]</sup>F)FDG uptake).<sup>59</sup> We focused our *a priori* analyses in both humans and mice on the circuit between the basal forebrain and EC based on reported early issues with EC-related functions.<sup>19,21</sup> Our results are consistent with the hypothesis that loss of EC cholinergic terminal density might underlie some of the earliest phases of age-related cognitive decline. At these early stages of EC-related cognitive impairment, loss of cholinergic terminal density in the EC might precede and be decoupled from amyloid plaque accumulation. As such, we propose that the EC-specific cholinergic deficits likely precede the more robust global cortical deficits found in previous studies. Our ongoing longitudinal studies with larger cohorts of participants and improved PET resolution are investigating the importance of LEC-specific cholinergic terminal integrity as the earliest predictive factor of future cognitive impairment. We suggest that VACHT density as assessed by <sup>[18]</sup>F)VAT could be useful as an early predictive measure of cognitive impairment.

**Conclusions**

In a series of translational experiments in healthy aging humans, healthy aging mice, and in genetically modified mice with aggravated expression of AD pathology, we present data supporting loss of cholinergic innervation in the LEC and loss of function of LEC-projecting cholinergic neurons as an early phenomenon intimately related to early cognitive decline. Furthermore, we reveal an important role for acetylcholine in normal EC functional engagement and object location memory. Our data suggest that EC VACHT availability may be a sensitive biomarker for early detection and potential intervention in age-related cognitive decline. If the goal of the field is to find biomarkers for early intervention, it seems we are still looking too late! At this early stage of cognitive impairment, the BFCN → EC circuit is already affected. Using these valuable *in vivo* imaging tools, supported by parallel preclinical assessment, studies that evaluate the onset of the cholinergic lesion and understand the predictive capability of VACHT density in diagnosing future cognitive impairment are needed. In addition, these data highlight that changes to cholinergic circuits are not homogeneous and occur at different rates. This concept falls in line with a growing body of

literature supporting the heterogeneity of different central cholinergic populations.<sup>1,62,63</sup> Understanding which factors confer resilience and vulnerability to cholinergic circuits may be key in maintaining cognition over the long term.

### Limitations of the study

Recent human studies identify the aLEC as the site of onset for age-related changes to the EC.<sup>13,15,17</sup> Discrimination of these anatomical and functional subdivisions of the EC requires higher-resolution imaging than achievable in our human PET studies. As such, we did not have the ability to evaluate whether the loss of integrity of the cholinergic system in OA-I participants was driven by changes in the aLEC specifically. In addition, in the human studies, we were unable to evaluate the importance of amyloid and tau pathology on cholinergic system deterioration and EC function. These limitations were addressed in part in the associated mouse studies and are currently being addressed in humans in ongoing studies. Further, while we designed our translational study to ask parallel questions across species, it should be noted that it is difficult to appropriately stage mouse age with human age and even more challenging to model all aspects of the human condition in a single mouse line. We attempted to overcome these limitations with evaluation of this circuit in more than one mouse model. Despite this, additional time points/ages are needed to better establish a time course of deterioration for the BFCN → EC circuit.

### RESOURCE AVAILABILITY

#### Lead contact

Requests for further information and resources should be directed to and will be fulfilled by the lead contact, Mala Ananth ([mala.ananth@nih.gov](mailto:mala.ananth@nih.gov)).

#### Materials availability

This study did not generate new unique reagents.

#### Data and code availability statement

- All datasets generated and analyzed in this study are available from the [lead contact](#) upon request.
- This study does not report original code.
- Any additional information required to reanalyze the data reported in this paper is available from the [lead contact](#) upon request.

### ACKNOWLEDGMENTS

The human studies presented in this paper were supported by funds from the Alzheimer's Foundation of America (C.D.) and internal pilot funds from Stony Brook University's Department of Psychiatry and Department of Radiology (M.R.A.). The rodent studies presented in this paper were supported by the National Institute of Neurological Disorders and Stroke Intramural Research Program (1ZIANS009416 and 1ZIANS009422 to L.W.R. and 1ZIANS009424 to D.A.T.) and early phases by NS022061 (to L.W.R.). L.Z. was supported by 2RF1NS023945-28. We would like to thank Dr. Xiang Zhang, Dr. Zhude Tu, and Dr. Joel Perlmuter for support initiating <sup>18</sup>F-VAT studies at Stony Brook University. We would like to thank Michala Godstrey, Natalka Haubold, Nichole Hoehn, Colleen Oliva, and Greg Perlman for help during the intake session of the human studies. For help with human PET/MR studies and tracer metabolite analysis, we would like to thank Fabrice Blain, Wayne Dinizio, Doyoung Noh, Sasha Russ, James Vulpi, George Wright, and Eunbin (Grace) Yoon. For help with human genotyping data, we would like to thank the Stony Brook University Genomics Core. We would also like to thank Dr. William Van Nostrand and Sukumar Vijayaraghavan for providing reagents for the rodent experiments described in this study. Figures were prepared with biorender.com.

### AUTHOR CONTRIBUTIONS

Conceptualization, M.R.A., L.W.R., D.A.T., C.D., and R.V.P.; methodology, M.R.A., J.D.G., M.S., C.D., R.V.P., L.W.R., and D.A.T.; software, J.D.G., M.R.A., and M.S.; formal analysis, M.R.A., J.D.G., and M.S.; investigation, M.R.A.; resources, M.R.A., M.S., N.P., C.H., L.Z., C.D., L.W.R., D.A.T., and R.V.P.; data curation, M.R.A. and J.D.G.; writing – review & editing, M.R.A., L.W.R., D.A.T., C.D., and R.V.P.; visualization, M.R.A., L.W.R., D.A.T., and C.D.; supervision, L.W.R., D.A.T., C.D., and R.V.P.; funding acquisition, C.D., L.W.R., D.A.T., R.V.P., and M.R.A.

### DECLARATION OF INTERESTS

The authors declare no competing interests.

### STAR METHODS

Detailed methods are provided in the online version of this paper and include the following:

- [KEY RESOURCES TABLE](#)
- [EXPERIMENTAL MODEL AND STUDY PARTICIPANT DETAILS](#)
  - Human subjects
  - Animal use
- [METHOD DETAILS](#)
  - Procedures & cognitive testing
  - PET/MRI scanning procedures
  - Mouse tissue handling procedures
- [QUANTIFICATION AND STATISTICAL ANALYSIS](#)
  - Human PET/MRI image processing

### SUPPLEMENTAL INFORMATION

Supplemental information can be found online at <https://doi.org/10.1016/j.celrep.2025.115249>.

Received: May 31, 2024

Revised: November 15, 2024

Accepted: January 9, 2025

Published: January 30, 2025

### REFERENCES

1. Ananth, M.R., Rajebhosale, P., Kim, R., Talmage, D.A., and Role, L.W. (2023). Basal forebrain cholinergic signalling: development, connectivity and roles in cognition. *Nat. Rev. Neurosci.* 24, 233–251. <https://doi.org/10.1038/s41583-023-00677-x>.
2. Gielow, M.R., and Zaborszky, L. (2017). The Input-Output Relationship of the Cholinergic Basal Forebrain. *Cell Rep.* 18, 1817–1830. <https://doi.org/10.1016/j.celrep.2017.01.060>.
3. Zaborszky, L., Duque, A., Gielow, M., Gombkoto, P., Nadasdy, Z., and Somogyi, J. (2015). Chapter 19 - Organization of the Basal Forebrain Cholinergic Projection System: Specific or Diffuse? In *The Rat Nervous System*, Fourth Edition, G. Paxinos, ed. (Academic Press), pp. 491–507. <https://doi.org/10.1016/B978-0-12-374245-2.00019-X>.
4. Záboršký, L., Gombkoto, P., Varsányi, P., Gielow, M.R., Poe, G., Role, L.W., Ananth, M., Rajebhosale, P., Talmage, D.A., Hasselmo, M.E., et al. (2018). Specific Basal Forebrain-Cortical Cholinergic Circuits Coordinate Cognitive Operations. *J. Neurosci.* 38, 9446–9458. <https://doi.org/10.1523/JNEUROSCI.1676-18.2018>.
5. Geula, C., Dunlop, S.R., Ayala, I., Kawles, A.S., Flanagan, M.E., Gefen, T., and Mesulam, M.M. (2021). Basal forebrain cholinergic system in the dementias: Vulnerability, resilience, and resistance. *J. Neurochem.* 158, 1394–1411. <https://doi.org/10.1111/jnc.15471>.

6. Geula, C., and Mesulam, M.-M. (1996). Systematic Regional Variations in the Loss of Cortical Cholinergic Fibers in Alzheimer's Disease. *Cerebr. Cortex* 6, 165–177. <https://doi.org/10.1093/cercor/6.2.165>.
7. Geula, C., and Mesulam, M.M. (1989). Cortical cholinergic fibers in aging and Alzheimer's disease: A morphometric study. *Neuroscience* 33, 469–481. [https://doi.org/10.1016/0306-4522\(89\)90399-0](https://doi.org/10.1016/0306-4522(89)90399-0).
8. Geula, C., Nagykery, N., Nicholas, A., and Wu, C.K. (2008). Cholinergic neuronal and axonal abnormalities are present early in aging and in Alzheimer disease. *J. Neuropathol. Exp. Neurol.* 67, 309–318. <https://doi.org/10.1097/NEN.0b013e31816a1df3>.
9. Igarashi, K.M. (2023). Entorhinal cortex dysfunction in Alzheimer's disease. *Trends Neurosci.* 46, 124–136. <https://doi.org/10.1016/j.tins.2022.11.006>.
10. Basu, J., and Siegelbaum, S.A. (2015). The Corticohippocampal Circuit, Synaptic Plasticity, and Memory. *Cold Spring Harbor Perspect. Biol.* 7, a021733. <https://doi.org/10.1101/cshperspect.a021733>.
11. Buszaki, G., and Moser, E.I. (2013). Memory, navigation and theta rhythm in the hippocampal-entorhinal system. *Nat. Neurosci.* 16, 130–138. <https://doi.org/10.1038/nn.3304>.
12. Braak, H., Alafuzoff, I., Arzberger, T., Kretschmar, H., and Del Tredici, K. (2006). Staging of Alzheimer disease-associated neurofibrillary pathology using paraffin sections and immunocytochemistry. *Acta Neuropathol.* 112, 389–404. <https://doi.org/10.1007/s00401-006-0127-z>.
13. Adams, J.N., Maass, A., Harrison, T.M., Baker, S.L., and Jagust, W.J. (2019). Cortical tau deposition follows patterns of entorhinal functional connectivity in aging. *Elife* 8, e49132. <https://doi.org/10.7554/elife.49132>.
14. Devanand, D.P., Pradhaban, G., Liu, X., Khandji, A., De Santi, S., Segal, S., Rusinek, H., Pelton, G.H., Honig, L.S., Mayeux, R., et al. (2007). Hippocampal and entorhinal atrophy in mild cognitive impairment: prediction of Alzheimer disease. *Neurology* 68, 828–836. <https://doi.org/10.1212/01.wnl.0000256697.20968.d7>.
15. Khan, U.A., Liu, L., Provenzano, F.A., Berman, D.E., Profaci, C.P., Sloan, R., Mayeux, R., Duff, K.E., and Small, S.A. (2014). Molecular drivers and cortical spread of lateral entorhinal cortex dysfunction in preclinical Alzheimer's disease. *Nat. Neurosci.* 17, 304–311. <https://doi.org/10.1038/nrn.3606>.
16. Kulason, S., Xu, E., Tward, D.J., Bakker, A., Albert, M., Younes, L., and Miller, M.I. (2020). Entorhinal and Transentorhinal Atrophy in Preclinical Alzheimer's Disease. *Front. Neurosci.* 14, 804. <https://doi.org/10.3389/fnins.2020.00804>.
17. Holbrook, A.J., Tustison, N.J., Marquez, F., Roberts, J., Yassa, M.A., and Gillen, D.L.; Alzheimer's Disease Neuroimaging Initiative (2020). Antero-lateral entorhinal cortex thickness as a new biomarker for early detection of Alzheimer's disease. *Alzheimers Dement.* 12, e12068. <https://doi.org/10.1002/dad2.12068>.
18. Kaufman, S.K., Del Tredici, K., Thomas, T.L., Braak, H., and Diamond, M.I. (2018). Tau seeding activity begins in the transentorhinal/entorhinal regions and anticipates phospho-tau pathology in Alzheimer's disease and PART. *Acta Neuropathol.* 136, 57–67. <https://doi.org/10.1007/s00401-018-1855-6>.
19. Reagh, Z.M., and Yassa, M.A. (2014). Object and spatial mnemonic interference differentially engage lateral and medial entorhinal cortex in humans. *Proc. Natl. Acad. Sci. USA* 111, E4264–E4273. <https://doi.org/10.1073/pnas.1411250111>.
20. Tran, T.T., Speck, C.L., Gallagher, M., and Bakker, A. (2022). Lateral entorhinal cortex dysfunction in amnestic mild cognitive impairment. *Neurobiol. Aging* 112, 151–160. <https://doi.org/10.1016/j.neurobiolaging.2021.12.008>.
21. Yeung, L.K., Olsen, R.K., Hong, B., Mihajlovic, V., D'Angelo, M.C., Kacolia, A., Ryan, J.D., and Barense, M.D. (2019). Object-in-place Memory Predicted by Anterolateral Entorhinal Cortex and Parahippocampal Cortex Volume in Older Adults. *J. Cognit. Neurosci.* 31, 711–729. [https://doi.org/10.1162/jocn\\_a\\_01385](https://doi.org/10.1162/jocn_a_01385).
22. Heys, J.G., Schultheiss, N.W., Shay, C.F., Tsuno, Y., and Hasselmo, M.E. (2012). Effects of acetylcholine on neuronal properties in entorhinal cortex. *Front. Behav. Neurosci.* 6, 32. <https://doi.org/10.3389/fnbeh.2012.00032>.
23. Nasreddine, Z.S., Phillips, N.A., Bédirian, V., Charbonneau, S., Whitehead, V., Collin, I., Cummings, J.L., and Chertkow, H. (2005). The Montreal Cognitive Assessment, MoCA: A Brief Screening Tool For Mild Cognitive Impairment. *J. Am. Geriatr. Soc.* 53, 695–699. <https://doi.org/10.1111/j.1532-5415.2005.53221.x>.
24. Moore, T.M., Reise, S.P., Gur, R.E., Hakonarson, H., and Gur, R.C. (2015). Psychometric properties of the Penn Computerized Neurocognitive Battery. *Neuropsychology* 29, 235–246. <https://doi.org/10.1037/neu0000093>.
25. Okada, K., Hashimoto, K., and Kobayashi, K. (2022). Cholinergic regulation of object recognition memory. *Front. Behav. Neurosci.* 16, 996089. <https://doi.org/10.3389/fnbeh.2022.996089>.
26. Van Cauter, T., Camon, J., Alvernhe, A., Elduayen, C., Sargolini, F., and Save, E. (2013). Distinct roles of medial and lateral entorhinal cortex in spatial cognition. *Cerebr. Cortex* 23, 451–459. <https://doi.org/10.1093/cercor/bhs033>.
27. Tu, Z., Zhang, X., Jin, H., Yue, X., Padakanti, P.K., Yu, L., Liu, H., Flores, H.P., Kaneshige, K., Parsons, S.M., and Perlmuter, J.S. (2015). Synthesis and biological characterization of a promising F-18 PET tracer for vesicular acetylcholine transporter. *Bioorg. Med. Chem.* 23, 4699–4709. <https://doi.org/10.1016/j.bmc.2015.05.058>.
28. Jin, H., Yue, X., Liu, H., Han, J., Flores, H., Su, Y., Parsons, S.M., Perlmuter, J.S., and Tu, Z. (2018). Kinetic modeling of [<sup>18</sup>F]VAT, a novel radioligand for positron emission tomography imaging vesicular acetylcholine transporter in non-human primate brain. *J. Neurochem.* 144, 791–804. <https://doi.org/10.1111/jnc.14291>.
29. Karimi, M., Tu, Z., Yue, X., Zhang, X., Jin, H., Perlmuter, J.S., and Laforest, R. (2015). Radiation dosimetry of [<sup>18</sup>F]JVT in nonhuman primates. *EJNMMI Res.* 5, 73. <https://doi.org/10.1186/s13550-015-0149-4>.
30. O'Donnell, J.L., Soda, A.K., Jiang, H., Norris, S.A., Maiti, B., Karimi, M., and Perlmuter, J.S. (2024). PET Quantification of [<sup>18</sup>F] VAT in Human Brain and Its Test-Retest Reproducibility and Age Dependence. *J. Nucl. Med.* 65, 956–961.
31. Knox, D., and Keller, S.M. (2016). Cholinergic neuronal lesions in the medial septum and vertical limb of the diagonal bands of Broca induce contextual fear memory generalization and impair acquisition of fear extinction. *Hippocampus* 26, 718–726. <https://doi.org/10.1002/hipo.22553>.
32. Kondo, H., and Zaborszky, L. (2016). Topographic organization of the basal forebrain projections to the perirhinal, postrhinal, and entorhinal cortex in rats. *J. Comp. Neurol.* 524, 2503–2515. <https://doi.org/10.1002/cne.23967>.
33. Zaborszky, L., Hoemke, L., Mohlberg, H., Schleicher, A., Amunts, K., and Zilles, K. (2008). Stereotaxic probabilistic maps of the magnocellular cell groups in human basal forebrain. *Neuroimage* 42, 1127–1141. <https://doi.org/10.1016/j.neuroimage.2008.05.055>.
34. Colton, C.A., Vitek, M.P., Wink, D.A., Xu, Q., Cantillana, V., Previti, M.L., Van Nostrand, W.E., Weinberg, J.B., and Dawson, H. (2006). NO synthase 2 (NOS2) deletion promotes multiple pathologies in a mouse model of Alzheimer's disease. *Proc. Natl. Acad. Sci. USA* 103, 12867–12872. <https://doi.org/10.1073/pnas.0601075103>.
35. Colton, C.A., Wilcock, D.M., Wink, D.A., Davis, J., Van Nostrand, W.E., and Vitek, M.P. (2008). The effects of NOS2 gene deletion on mice expressing mutated human AbetaPP. *J. Alzheimers Dis.* 15, 571–587. <https://doi.org/10.3233/JAD-2008-15405>.
36. Wilcock, D.M., Lewis, M.R., Van Nostrand, W.E., Davis, J., Previti, M.L., Gharkholonarehe, N., Vitek, M.P., and Colton, C.A. (2008). Progression of amyloid pathology to Alzheimer's disease pathology in an amyloid precursor protein transgenic mouse model by removal of nitric oxide synthase 2. *J. Neurosci.* 28, 1537–1545. <https://doi.org/10.1523/jneurosci.5066-07.2008>.

37. Grybko, M.J., Hahm, E.T., Perrine, W., Parnes, J.A., Chick, W.S., Sharma, G., Finger, T.E., and Vijayaraghavan, S. (2011). A transgenic mouse model reveals fast nicotinic transmission in hippocampal pyramidal neurons. *Eur. J. Neurosci.* 33, 1786–1798. <https://doi.org/10.1111/j.1460-9568.2011.07671.x>.
38. Tsao, A., Moser, M.B., and Moser, E.I. (2013). Traces of experience in the lateral entorhinal cortex. *Curr. Biol.* 23, 399–405. <https://doi.org/10.1016/j.cub.2013.01.036>.
39. Save, E., and Sargolini, F. (2017). Disentangling the Role of the MEC and LEC in the Processing of Spatial and Non-Spatial Information: Contribution of Lesion Studies. *Front. Syst. Neurosci.* 11, 81. <https://doi.org/10.3389/fnsys.2017.00081>.
40. Parron, C., Poucet, B., and Save, E. (2006). Cooperation between the hippocampus and the entorhinal cortex in spatial memory: a disconnection study. *Behav. Brain Res.* 170, 99–109. <https://doi.org/10.1016/j.bbr.2006.02.006>.
41. Mesulam, M.M. (2013). Cholinergic circuitry of the human nucleus basalis and its fate in Alzheimer's disease. *J. Comp. Neurol.* 521, 4124–4144. <https://doi.org/10.1002/cne.23415>.
42. Mesulam, M.M., Mufson, E.J., Levey, A.I., and Wainer, B.H. (1983). Cholinergic innervation of cortex by the basal forebrain: cytochemistry and cortical connections of the septal area, diagonal band nuclei, nucleus basalis (substantia innominata), and hypothalamus in the rhesus monkey. *J. Comp. Neurol.* 214, 170–197. <https://doi.org/10.1002/cne.902140206>.
43. Liu, C.-C., Liu, C.C., Kanekiyo, T., Xu, H., and Bu, G. (2013). Apolipoprotein E and Alzheimer disease: risk, mechanisms and therapy. *Nat. Rev. Neurol.* 9, 106–118. <https://doi.org/10.1038/nrneurol.2012.263>.
44. Wisniewski, T., and Drummond, E. (2020). APOE-amyloid interaction: Therapeutic targets. *Neurobiol. Dis.* 138, 104784. <https://doi.org/10.1016/j.nbd.2020.104784>.
45. Bertram, L., and Tanzi, R.E. (2009). Genome-wide association studies in Alzheimer's disease. *Hum. Mol. Genet.* 18, R137–R145. <https://doi.org/10.1093/hmg/ddp406>.
46. Okkels, N., Horsager, J., Labrador-Espinosa, M.A., Hansen, F.O., Andersen, K.B., Just, M.K., Fedorova, T.D., Skjærbaek, C., Munk, O.L., Hansen, K.V., et al. (2023). Distribution of cholinergic nerve terminals in the aged human brain measured with [18F]FEOBV PET and its correlation with histological data. *Neuroimage* 269, 119908. <https://doi.org/10.1016/j.neuroimage.2023.119908>.
47. Schmitz, T.W., Mur, M., Aghourian, M., Bedard, M.A., and Spreng, R.N.; Alzheimer's Disease Neuroimaging Initiative (2018). Longitudinal Alzheimer's Degeneration Reflects the Spatial Topography of Cholinergic Basal Forebrain Projections. *Cell Rep.* 24, 38–46. <https://doi.org/10.1016/j.celrep.2018.06.001>.
48. Sexton, C.E., Kalu, U.G., Filippini, N., Mackay, C.E., and Ebmeier, K.P. (2011). A meta-analysis of diffusion tensor imaging in mild cognitive impairment and Alzheimer's disease. *Neurobiol. Aging* 32, 2322–2325. <https://doi.org/10.1016/j.neurobiolaging.2010.05.019>.
49. Madden, D.J., Bennett, I.J., Burzynska, A., Potter, G.G., Chen, N.-K., and Song, A.W. (2012). Diffusion tensor imaging of cerebral white matter integrity in cognitive aging. *Biochim. Biophys. Acta* 1822, 386–400. <https://doi.org/10.1016/j.bbadiis.2011.08.003>.
50. Manns, I.D., Mainville, L., and Jones, B.E. (2001). Evidence for glutamate, in addition to acetylcholine and GABA, neurotransmitter synthesis in basal forebrain neurons projecting to the entorhinal cortex. *Neuroscience* 107, 249–263. [https://doi.org/10.1016/s0306-4522\(01\)00302-5](https://doi.org/10.1016/s0306-4522(01)00302-5).
51. Desikan, S., Koser, D.E., Neitz, A., and Monyer, H. (2018). Target selectivity of septal cholinergic neurons in the medial and lateral entorhinal cortex. *Proc. Natl. Acad. Sci. USA* 115, E2644–E2652. <https://doi.org/10.1073/pnas.1716531115>.
52. Petrache, A.L., Rajulawalla, A., Shi, A., Wetzel, A., Saito, T., Saido, T.C., Harvey, K., and Ali, A.B. (2019). Aberrant Excitatory-Inhibitory Synaptic Mechanisms in Entorhinal Cortex Microcircuits During the Pathogenesis of Alzheimer's Disease. *Cerebr. Cortex* 29, 1834–1850. <https://doi.org/10.1093/cercor/bhz016>.
53. Targa Dias Anastacio, H., Matosin, N., and Ooi, L. (2022). Neuronal hyperexcitability in Alzheimer's disease: what are the drivers behind this aberrant phenotype? *Transl. Psychiatry* 12, 257. <https://doi.org/10.1038/s41398-022-02024-7>.
54. Busche, M.A., Eichhoff, G., Adelsberger, H., Abramowski, D., Wiederhold, K.H., Haass, C., Staufenbiel, M., Konnerth, A., and Garaschuk, O. (2008). Clusters of hyperactive neurons near amyloid plaques in a mouse model of Alzheimer's disease. *Science* 321, 1686–1689. <https://doi.org/10.1126/science.1162844>.
55. Lawrence, J.J. (2008). Cholinergic control of GABA release: emerging parallels between neocortex and hippocampus. *Trends Neurosci.* 31, 317–327. <https://doi.org/10.1016/j.tins.2008.03.008>.
56. Petrou, M., Frey, K.A., Kilbourn, M.R., Scott, P.J.H., Raffel, D.M., Bohnen, N.I., Müller, M.L.T.M., Albin, R.L., and Koepp, R.A. (2014). In Vivo Imaging of Human Cholinergic Nerve Terminals with ( $-$ ) $5\text{-}^{18}\text{F}$ -Fluoroethoxybenzovesamicol: Biodistribution, Dosimetry, and Tracer Kinetic Analyses. *J. Nucl. Med.* 55, 396–404. <https://doi.org/10.2967/jnumed.113.124792>.
57. Mulholland, G.K., Wieland, D.M., Kilbourn, M.R., Frey, K.A., Sherman, P.S., Carey, J.E., and Kuhl, D.E. (1998). [ $^{18}\text{F}$ ]fluoroethoxybenzovesamicol, a PET radiotracer for the vesicular acetylcholine transporter and cholinergic synapses. *Synapse* 30, 263–274. [https://doi.org/10.1002/\(SICI\)1098-2396\(199811\)30:3<263::AID-SYN4>3.0.CO;2-9](https://doi.org/10.1002/(SICI)1098-2396(199811)30:3<263::AID-SYN4>3.0.CO;2-9).
58. Kilbourn, M.R., Hockley, B., Lee, L., Sherman, P., Quesada, C., Frey, K.A., and Koepp, R.A. (2009). Positron emission tomography imaging of ( $2\text{R},3\text{R}$ )-5-[( $18\text{F}$ )fluoroethoxybenzovesamicol in rat and monkey brain: a radioligand for the vesicular acetylcholine transporter. *Nucl. Med. Biol.* 36, 489–493. <https://doi.org/10.1016/j.nucmedbio.2009.02.007>.
59. Aghourian, M., Legault-Denis, C., Soucy, J.P., Rosa-Neto, P., Gauthier, S., Kostikov, A., Gravel, P., and Bédard, M.A. (2017). Quantification of brain cholinergic denervation in Alzheimer's disease using PET imaging with [ $^{18}\text{F}$ ]-FEOBV. *Mol. Psychiatr.* 22, 1531–1538. <https://doi.org/10.1038/mp.2017.183>.
60. Xia, Y., Eeles, E., Fripp, J., Pinsker, D., Thomas, P., Latter, M., Doré, V., Fazlollahi, A., Bourgeat, P., Villemagne, V.L., et al. (2022). Reduced cortical cholinergic innervation measured using [ $^{18}\text{F}$ ]-FEOBV PET imaging correlates with cognitive decline in mild cognitive impairment. *Neuroimage. Clin.* 34, 102992. <https://doi.org/10.1016/j.nicli.2022.102992>.
61. Nejad-Davarani, S., Koepp, R.A., Albin, R.L., Frey, K.A., Müller, M.L.T.M., and Bohnen, N.I. (2019). Quantification of brain cholinergic denervation in dementia with Lewy bodies using PET imaging with [ $^{18}\text{F}$ ]-FEOBV. *Mol. Psychiatr.* 24, 322–327. <https://doi.org/10.1038/s41380-018-0130-5>.
62. Kim, R., Ananth, M., Desai, N.S., Role, L.W., and Talmage, D.A. (2023). Distinct subpopulations of ventral pallidal cholinergic projection neurons encode valence of olfactory stimuli. Preprint at bioRxiv 2023, 561261. <https://doi.org/10.1101/2023.10.06.561261>.
63. Rajebhosale, P., Ananth, M., Crouse, R., Jiang, L., Hernández, G.L.-., Arty, C., Wang, S., Jone, A., Zhong, C., Desai, N.S., et al. (2021). Basal forebrain cholinergic neurons are part of the threat memory engram. Preprint at bioRxiv 2021. <https://doi.org/10.1101/2021.05.02.442364>.
64. Gomez, J.L., Bonaventura, J., Lesniak, W., Mathews, W.B., Sysa-Shah, P., Rodriguez, L.A., Ellis, R.J., Richie, C.T., Harvey, B.K., Dannals, R.F., et al. (2017). Chemogenetics revealed: DREADD occupancy and activation via converted clozapine. *Science* 357, 503–507. <https://doi.org/10.1126/science.aan2475>.
65. Ladefoged, C.N., Law, I., Anazodo, U., St. Lawrence, K., Izquierdo-Garcia, D., Catana, C., Burgos, N., Cardoso, M.J., Urselin, S., Hutton, B., et al. (2017). A multi-centre evaluation of eleven clinically feasible brain PET/MRI attenuation correction techniques using a large cohort of patients. *Neuroimage* 147, 346–359. <https://doi.org/10.1016/j.neuroimage.2016.12.010>.

66. DeLorenzo, C., Klein, A., Mikhno, A., Gray, N., Zanderigo, F., Mann, J., and Parsey, R. (2009). A new method for assessing PET-MRI coregistration. In *Medical imaging 2009: image processing*, 7259 (SPIE), pp. 962–969.
67. Avants, B.B., Tustison, N.J., Wu, J., Cook, P.A., and Gee, J.C. (2011). An open source multivariate framework for n-tissue segmentation with evaluation on public data. *Neuroinformatics* 9, 381–400. <https://doi.org/10.1007/s12021-011-9109-y>.
68. Avants, B.B., Tustison, N.J., Song, G., Cook, P.A., Klein, A., and Gee, J.C. (2011). A reproducible evaluation of ANTs similarity metric performance in brain image registration. *Neuroimage* 54, 2033–2044. <https://doi.org/10.1016/j.neuroimage.2010.09.025>.
69. Duvernoy, H.M. (1999). *The Human Brain: Surface, Three-Dimensional Sectional Anatomy with MRI, and Blood Supply* (Springer Science & Business Media).
70. Talairach, P.J. (1988). Co-planar stereotaxic atlas of the human brain.
71. Kates, W.R., Abrams, M.T., Kaufmann, W.E., Breiter, S.N., and Reiss, A.L. (1997). Reliability and validity of MRI measurement of the amygdala and hippocampus in children with fragile X syndrome. *Psychiatr. Res.* 75, 31–48.
72. Killiany, R.J., Moss, M.B., Nicholson, T., Jolesz, F., and Sandor, T. (1997). An interactive procedure for extracting features of the brain from magnetic resonance images: the lobes. *Hum. Brain Mapp.* 5, 355–363.
73. Ogden, R.T., Ojha, A., Erlandsson, K., Oquendo, M.A., Mann, J.J., and Parsey, R.V. (2007). In vivo quantification of serotonin transporters using [(11)C]DASB and positron emission tomography in humans: modeling considerations. *J. Cerebr. Blood Flow Metabol.* 27, 205–217. <https://doi.org/10.1038/sj.jcbfm.9600329>.
74. Ardekani, B.A., Guckemus, S., Bachman, A., Hoptman, M.J., Wojtaszek, M., and Nierenberg, J. (2005). Quantitative comparison of algorithms for inter-subject registration of 3D volumetric brain MRI scans. *J. Neurosci. Methods* 142, 67–76. <https://doi.org/10.1016/j.jneumeth.2004.07.014>.
75. Erlandsson, K., Buvat, I., Pretorius, P.H., Thomas, B.A., and Hutton, B.F. (2012). A review of partial volume correction techniques for emission tomography and their applications in neurology, cardiology and oncology. *Phys. Med. Biol.* 57, R119–R159. <https://doi.org/10.1088/0031-9155/57/21/r119>.
76. Yang, J., Huang, S.C., Mega, M., Lin, K.P., Toga, A.W., Small, G.W., and Phelps, M.E. (1996). Investigation of partial volume correction methods for brain FDG PET studies. *IEEE Trans. Nucl. Sci.* 43, 3322–3327. <https://doi.org/10.1109/23.552745>.
77. Thomas, B.A., Cuplov, V., Bousse, A., Mendes, A., Thielemans, K., Hutton, B.F., and Erlandsson, K. (2016). PETPVC: a toolbox for performing partial volume correction techniques in positron emission tomography. *Phys. Med. Biol.* 61, 7975–7993. <https://doi.org/10.1088/0031-9155/61/22/7975>.
78. Innis, R.B., Cunningham, V.J., Delforge, J., Fujita, M., Gjedde, A., Gunn, R.N., Holden, J., Houle, S., Huang, S.-C., Ichise, M., et al. (2007). Consensus Nomenclature for *in vivo* Imaging of Reversibly Binding Radioligands. *J. Cerebr. Blood Flow Metabol.* 27, 1533–1539. <https://doi.org/10.1038/sj.jcbfm.9600493>.
79. Gray, C.M., Maldonado, P.E., Wilson, M., and McNaughton, B. (1995). Tetrodes markedly improve the reliability and yield of multiple single-unit isolation from multi-unit recordings in cat striate cortex. *J. Neurosci. Methods* 63, 43–54.

## STAR★METHODS

### KEY RESOURCES TABLE

| REAGENT or RESOURCE                                     | SOURCE  | IDENTIFIER  |
|---|---|---|
| <b>Antibodies</b>                                       |   |   |
| Goat Anti-Choline Acetyltransferase                     | Millipore   | CAT# AB114P; RRID: AB_2079751   |
| Rabbit Anti-Vesicular Acetylcholine Transporter         | Synaptic Systems  | CAT# 139103; RRID:AB_887864   |
| Guinea Pig Anti cFos                                    | Synaptic Systems  | CAT# 226004; RRID:AB_2619946  |
| Mouse-AT8   | ThermoFisher  | Cat# MN1020; RRID:AB_223647   |
| GP Anti-ABeta   | Synaptic Systems  | Cat# 218308; RRID:AB_2744642  |
| Donkey Anti Goat, IgG, Alexa Fluor Plus 488             | ThermoFisher  | Cat# A32814; RRID:AB_2762838  |
| Donkey Anti Rabbit, IgG, Alexa Fluor Plus 647           | ThermoFisher  | Cat# A32795; RRID:AB_2762835  |
| Donkey Anti Mouse, IgG, Alexa Fluor Plus 594            | ThermoFisher  | Cat# A32744; RRID:AB_2762826  |
| Donkey Anti Guinea Pig, IgG, Alexa Fluor 488 AffiniPure | Jackson ImmunoResearch  | Cat# 106-545-003; RRID:AB_2337438   |
| Donkey Anti Guinea Pig, IgG, Alexa Fluor 594 AffiniPure | Jackson ImmunoResearch  | Cat# 106-585-003; RRID:AB_2337442   |
| Donkey Anti Guinea Pig, IgG, Alexa Fluor 647 AffiniPure | Jackson ImmunoResearch  | Cat# 106-605-003; RRID:AB_2337446   |
| <b>Bacterial and virus strains</b>                      |   |   |
| CAV2-DIO-hM4Di-mCherry                                  | Dr. EJ Kremer, Institut de Génétique Moléculaire de Montpellier, France | N/A   |
| AAV9-camk2a-GCaMP6f-WPRE-SV40                           | Penn Vector Core  | N/A   |
| <b>Chemicals, peptides, and recombinant proteins</b>    |   |   |
| Fast Blue   | Polysciences Inc  | Cat#17740-1   |
| Clozapine   | Sigma   | Cat #C6305  |
| Normal Donkey Serum                                     | Jackson Immuno Research   | Cat # 017-000-121   |
| Fluoromount-G with DAPI                                 | Southern Bio Tech   | Cat # 0100-01   |
| [ <sup>18</sup> F]VAT radiotracer                       | Jin et al. 2018, Weinstein et al. 2024, and This Paper                  | N/A   |
| <b>Experimental models: Organisms/strains</b>           |   |   |
| Mouse: C57BL/6J   | The Jackson Laboratory  | Jax Strain # 000664   |
| Mouse: Chat-IRES-Cre:Δneo                               | The Jackson Laboratory  | Jax Strain # 031661   |
| Mouse: ChAT-tau-eGFP                                    | From S.Vijayaraghavan, University of Colorado                           | N/A   |
| Mouse: 5XFAD  | The Jackson Laboratory  | Jax Strain # 34840  |
| Mouse: NOS2 <sup>-/-</sup>                              | The Jackson Laboratory  | Jax Strain # 002609   |
| <b>Software and algorithms</b>                          |   |   |
| MATLAB (2020a)  | Mathworks   | <a href="https://www.mathworks.com/products/matlab.html">https://www.mathworks.com/products/matlab.html</a> ; RRID:SCR_001622 |
| Imaris  | Oxford Instruments  | <a href="https://imaris.oxinst.com/">https://imaris.oxinst.com/</a> ; RRID:SCR_007370   |
| EthoVision XT (v 15)                                    | Noldus  | <a href="https://www.noldus.com/ethovision-xt">https://www.noldus.com/ethovision-xt</a> ; RRID:SCR_000441                     |
| Graphpad Prism (v 10)                                   | Graphpad  | <a href="https://www.graphpad.com/features">https://www.graphpad.com/features</a> ; RRID:SCR_002798                           |
| SPSS (V21)  | IBM   | N/A   |
| PennCNB Battery   | University of Pennsylvania  | <a href="https://webcnb.med.upenn.edu/">https://webcnb.med.upenn.edu/</a>   |
| FreeSurfer  | Harvard University  | <a href="https://surfer.nmr.mgh.harvard.edu/">https://surfer.nmr.mgh.harvard.edu/</a>   |
| DSI Studio  | Frank Yeh   | <a href="https://dsi-studio.labsolver.org/">https://dsi-studio.labsolver.org/</a>   |
| PETPVC ToolBox  | Thomas et al. 2016  | <a href="https://github.com/UCL/PETPVC">https://github.com/UCL/PETPVC</a>   |

**EXPERIMENTAL MODEL AND STUDY PARTICIPANT DETAILS****Human subjects**

This study was approved by the Institutional Review Board at Stony Brook University. All participants provided written informed consent. Recruitment took place between September 2017 and June 2019.

Participants for the human study were recruited from the local community based on the following inclusion criteria: 1) Age between 50 and 85 years; 2) Capacity to consent; 3) Under 275 lbs (based on scanner bed weight limits). Exclusion criteria included: 1) Significant physical illness; 2) History of DSM-V disorder excluding substance use or dependence; 3) Current substance use disorder; IV drug use in the past 5 years, MDMA use more than 10 times in 5 years; 4) Nicotine use, including tobacco, e-cigarettes, nicotine patch, nicotine gum, or lozenges in the past year; 5) Women who are premenopausal or not surgically sterile; 6) Unable to stop drugs or medication that affect cognition including those that affect the cholinergic system; 7) Current, past, or anticipated exposure to radiation including being badged for work, participation in nuclear medicine procedures, or recent exposure to multiple radiographic images that would exceed yearly exposure limits; 8) Any MRI contraindications including claustrophobia, metal implants, pacemakers, ICDs; 9) Blood donation within 8 weeks of the start of the study; 10) History of head trauma with prolonged loss of consciousness or any neurological condition; 11) Medicinal patch that could not be removed; 12) Anticoagulant or anti-platelet treatment other than aspirin. Fourteen participants were recruited into the study and signed informed consent forms. Subjects were divided into two groups based on performance on the clinical criteria for the Montreal Cognitive Assessment (administered during the intake session): Older Adults (OA) presented with a MoCA score of 26 or greater; Impaired Older Adults (OA-I) presented with a MoCA score of less than 26. One OA participant did not complete the PET study procedures and was excluded from PET analyses. One OA-I participant did not complete PET and MRI study procedures and was excluded from PET and MRI analyses. These participants were included in the reporting of cognitive testing measures. Blood samples from 8 participants (4 OA and 4 OA-I) underwent genotyping for ApoE status by identification of the following polymorphisms: rs429358 and rs7412. Experimenters were blinded to genotyping results until after all analyses were completed. These results are reported in the sample characteristics table ([Table S1](#)).

**Animal use**

Male and female mice between the ages of 1.5 and 6 months were used for the reported experiments. The following strains were used in the generation of this data: C57BL/6J (Jax stock number 000664), 5XFAD (Jax stock number 34840), NOS2<sup>-/-</sup> (Jax stock number 002609), Chat-ires-CreΔneo (Jax stock number 031661), and ChAT-tau:eGFP (Sukumar Vijayaraghavan<sup>37</sup>). Aβ<sup>+</sup>Tau<sup>+</sup> animals were the offspring of crosses between 5XFAD<sup>+/+</sup>/NOS2<sup>-/-</sup> X NOS2<sup>-/-</sup>: 5XFAD<sup>+</sup> and 5XFAD<sup>-</sup> mice were used as Aβ<sup>+</sup>Tau<sup>+</sup> and littermate controls. All mice were maintained on a C57 background. Animals were housed in a 12 h light/dark cycle environment that was both temperature and humidity controlled. Animals had free access to food and water. Mice were either pair or group housed when possible. No single housed mice were used for behavioral experiments. All animal care and experimental procedures were approved by the Institutional Animal Care and Use Committees of the SUNY Research Foundation at Stony Brook University (1618) and the NINDS IRP (1490 and 1531).

**METHOD DETAILS****Procedures & cognitive testing****Clinical procedures**

All human participants underwent a structured clinical interview for DSM-V (SCID) by a graduate level rater for evaluation of DSM-V disorders or diagnoses. All participants underwent a series of cognitive testing including a Mini Mental State Examination (MMSE), Montreal Cognitive Assessment (MoCA), and Penn Computerized Neurocognitive Battery (PennCNB). Analysis focused on the spatial visual object learning task (SVOLT task) within the PennCNB. Performance score was calculated by evaluating the number of correct responses for each participant within each test session consisting of 30 trials (score out of 30).

**Mouse stereotaxic surgery**

Three-month-old ChAT-ires-Cre mice or ChAT-tau:eGFP mice were anesthetized and stereotactically injected (Kopf) bilaterally (200nL per site) in the lateral EC (−4.0 mm A/P, ±4.5mm D/V, −3.5 mm M/L, empirically determined using landmarks). Viruses: CAV2-DIOhM4Di. mCherry was obtained from Dr. E.J. Kremer (Institut de Génétique Moléculaire de Montpellier, France) and AAV9-PCaMKIIa-GCaMP6f.WPRE.SV40 (obtained from U.Penn Vector Core) to visualize the injection site. Retrograde tracing experiments were conducted via injection with Fast Blue (3% solution in sterile water w/v, Polysciences Inc). 80nL of 3% Fast Blue was injected into the lateral entorhinal cortex of WT animals bilaterally. Mice were euthanized 4 days after injection.

**Mouse displaced object recognition (DOR) task**

All mouse behavioral experiments were conducted in a dark room with overhead red-light lamps. The behavioral arenas used were 30 cm × 30 cm rectangular cages covered with a transparent lid. One arena was used for staging while the other was used for testing. Mice were transported to and from the home-cage using a transparent, plastic platform. The displaced object recognition task was conducted over five days. Each arena was wiped down with 70% ethanol or Clidox prior to the sessions to ensure the same scent was associated with each session and to eliminate the odor from any previous animal. Habituation took place on days one through four. Mice were habituated to both the staging and testing arenas as well as transport to and from the home cage. During habituation

sessions, mice were given 5 min in each chamber before being returned to the home cage. The staging arena was empty (open arena), whereas the testing arena consisted of three objects spaced throughout the chamber. On day five, one of the objects was moved to a different location within the testing arena. Test sessions were 5 min. The displaced object was counterbalanced to ensure there was no preference to one side of the arena. Behavior data was recorded with a Logitech webcam and subsequently analyzed using Ethovision Analysis.

For DREADD experiments, mice were administered 0.1 mg/kg Clozapine<sup>64</sup> (Sigma Aldrich) interperitoneally 10 min prior to the test session.

#### Mouse *in vivo* electrophysiology

Mice were anesthetized with isoflurane and placed on a heated surgical stereotaxic stage (Kopf instruments). Craniotomy was performed over the left entorhinal cortex and a 5 MOhm parylene-C insulated tungsten electrode (AM systems, Sequim, WA) was placed into the left lateral EC. Recordings were pre-amplified using a head-stage from an A-M Systems amplifier. Data was acquired at a sampling rate of 40kHz, filtered between 100 and 1000 Hz by an A-M Systems amplifier and a Humbug Noise Eliminator (A-M Systems), and input to a 1401 data acquisition board (Cambridge Electronic Design). All data were collected using the Spike 2 software (Cambridge Electronic Design).

#### PET/MRI scanning procedures

##### Radiosynthesis of [<sup>18</sup>F]VAT for *in vivo* human studies

[<sup>18</sup>F]VAT was prepared in a one-step synthesis using a GE Tracerlab FXN pro synthesis module. Briefly, [<sup>18</sup>F]fluoride was reacted with 2-((7-(4-(4-fluorobenzoyl)piperidin-1-yl)-6-hydroxy-5,6,7,8-tetrahydronaphthalen-1-yl)oxy)ethyl 4-methylbenzenesulfonate in acetonitrile. Unreacted [<sup>18</sup>F]fluoride was removed by passing the reaction mixture over an alumina SPE cartridge and [<sup>18</sup>F]VAT was separated from the other compounds in the reaction mixture using preparative high-performance liquid chromatography (HPLC) using a C18 column (Phenomenex, 250 × 10 mm, LunaR 10/ $\mu$ m C18(2) 100 Å) and a mobile phase of 0.1 M ammonium formate in 38% acetonitrile at a flow rate of 4 mL/min. The peak corresponding to [<sup>18</sup>F]VAT was collected and further purified by dilution with water and absorption onto a C18 solid phase extraction cartridge (SPE). The SPE was washed with water to remove traces of acetonitrile and buffer. The purified [<sup>18</sup>F]-VAT was then eluted with absolute ethanol and diluted with sterile 0.9% saline. The manufacturing process typically takes 1 h, and the typical decay corrected chemical yield was 20–30%. Specific activities at the end of synthesis were 4.04 ± 1.55 Ci/ $\mu$ mole and the radiochemical purity was >99%.

##### Human positron emission tomography protocol

A venous catheter was placed for injection of the radioisotope. An arterial catheter was placed in the opposite arm for collection of arterial blood samples for the duration of the scan. PET and MRI data were acquired on a simultaneous PET/MRI scanner, Siemens Biograph mMR (software version VB20P). Up to 5 mCi of [<sup>18</sup>F]VAT was administered intravenously as a bolus over 30 s. Emission data was collected in three-dimensional mode for 150 min post injection for 38 frames of increasing duration: 6 frames at 20sec, 6 frames at 1min, 6 frames at 2 min, 14 frames at 5 min, 6 frames at 10 min. PET data were reconstructed with the template-based Boston attenuation correction,<sup>65</sup> scatter correction and randoms correction. The intrinsic resolution of the scanner at the center of the field of view was 3 mm full width at half maximum.

##### Human MRI imaging protocol

T1-weighted structural MRI images were acquired using a magnetization-prepared rapid gradient-echo (MP RAGE) sampling sequence. All images were acquired simultaneously during the PET acquisition with a 20-channel head coil and the following parameters: TR/TE/TI = 2300/2.98/900 ms, Flip Angle = 9°, IPAT (integrated parallel acquisition technique) = 2, and voxel resolution: 0.87 × 0.87 × 0.87 mm<sup>3</sup>.

Diffusion MRI images were acquired using a multi-band EPI sequence with the following parameters: TR = 6300ms, TE = 121.4ms, flip angle = 78°, refocus flip angle = 160°, fat saturation, FOV = 224 × 216 × 128mm, base resolution = 112, bandwidth = 992 Hz/Px, voxel size = 2 × 2 × 2 mm<sup>3</sup>, multi-band acceleration factor = 2, 4 shells of diffusion vectors with b values = 1000, 2000, 3000, 4000 with 64, 64, 32, 32 diffusion directions respectively, and an acquisition time of 18:16 min.

##### PET metabolite & free fraction analysis

Arterial samples were collected with an automated sampling system (Swiss-Trace) continuously for the first 6 min and manually thereafter. Eleven arterial blood samples were obtained at 2, 6, 12, 18, 25, 30, 40, 50, 60, 120, and 150 min during each scan for measurement of the arterial plasma activity over time.

Seven plasma samples were manually obtained at 2, 6, 12, 18, 30, 60, and 120 min during each scan for the determination of intact and metabolized [<sup>18</sup>F]VAT. Samples of whole blood and plasma were weighed and counted in a gamma counter (PerkinElmer Wizard, 2480) to determine the clearance rate. Plasma proteins were precipitated with acetonitrile and the supernatant analyzed by HPLC (LabLogic Posiram BGO coincidence detector) using a C18 column (Phenomenex, 250 × 4 mm, LunaR 10/ $\mu$ m C18(2) 100 Å) and an eluent of 0.1M ammonium formate in 50% acetonitrile, at a flow rate of 1 mL/min. The free fraction was determined by spiking the participant's free plasma, pooled plasma and saline with [<sup>18</sup>F]VAT and incubating the mixture for 5 min. These samples were then centrifuged (Millipore, UltracelR PL) and samples of the original samples and the filtrates weighed and counted in a gamma counter (PerkinElmer Wizard 2480).

The seven unmetabolized parent fraction levels were fit with a Hill Function and weighted equally. This fit was then used to correct the plasma radioactivity (multiplied by the plasma data), which was fit as a straight line to the peak, and the sum of three-exponentials after the peak. The fitted values were used as input to subsequent analyses.

### Mouse tissue handling procedures

#### Mouse tissue processing

Following PFA perfusion, mouse brains were post-fixed overnight at 4°C in 4% PFA (in 1XPBS) and were then transferred to a 30% sucrose solution (in 1XPBS). Brains were flash frozen in OCT Compound (Tissue Tek) and stored at -80°C until cryosectioning. 50 µm cryosections were collected into a solution of 1:1 PBS:glycerol and stored at -20 until immunostaining and/or imaging procedures.

#### Tissue immunohistochemistry

Sections were blocked overnight at 4°C in a PBS solution containing 2.0% Triton X-100 and 10% normal donkey serum and then incubated with primary antibody in a PBS-T solution (2% Triton X-100 and 10% normal donkey serum), overnight (24 h at 4°C). The next day, sections were rinsed in PBS-T and incubated in secondary antibody for 2 h at room temperature in PBS-T solution (2% Triton X-100 and 10% normal donkey serum). Sections were mounted in Fluoromount- G (Southern Biotech). Primary Antibodies: Goat anti ChAT (Millipore, Cat# AB114P, 1:500), Rabbit Anti VACHT (Synaptic Systems, Cat# 139103, 1:500), Guinea-Pig Anti-cFos (Synaptic Systems, Cat# 226004, 1:500), Mouse-AT8 (Thermo Fisher, Cat# MN1020, 1:250), GP Anti ABeta (Synaptic Systems, Cat# 218308, 1:500). Secondary antibodies: Donkey anti Goat IgG, Alexa Fluor 488 (Thermo Fisher, Cat# A32814, 1:750), Donkey anti Rabbit IgG, Alexa Fluor 647 (Thermo Fisher, Cat# A32795 1:750), Donkey anti Mouse IgG, Alexa Fluor 594 (Thermo Fisher, Cat# A32744, 1:750), Alexa Fluor 647 AffiniPure Donkey Anti-Guinea Pig IgG (Jackson ImmunoResearch, Cat# 106-605-003, 1:750), Alexa Fluor 488 AffiniPure Donkey Anti-Guinea Pig IgG (Jackson ImmunoResearch, Cat# 106-545-003, 1:750), Alexa Fluor 594 AffiniPure Donkey Anti-Guinea Pig IgG (Jackson ImmunoResearch, Cat# 106-585-003, 1:750).

## QUANTIFICATION AND STATISTICAL ANALYSIS

#### Human PET/MRI image processing

Imaging analysis was processed through our custom Brain Analysis Toolbox (BAT) consisting of a series of processing steps for both the MRI and the PET image. To begin, the last PET 30 frames are registered to the eighth frame using the Functional Magnetic Resonance Imaging of the Brain's Linear Image Registration Tool (FLIRT; FMRIB Image Analysis Group, Oxford, UK) to correct for motion throughout the scan. Once the mean motion correction image is created, eight different registrations (between the mean PET image and the MRI) are considered using different weighting schemes as previously described.<sup>66</sup> Subject MRIs were preprocessed with SPM for segmentation (into gray matter, white matter, and CSF; Statistical Parametric Mapping, Wellcome Center for Human Neuroimaging) and an automated skull-stripping algorithm (Atropos).<sup>67</sup> After the optimal registration is chosen based on a mutual information metric and manual verification, the coregistration is applied to all PET frames and images are registered to the higher resolution MRI.

Three atlases were used in the quantification of regions reported in this manuscript. Entorhinal cortex (EC) regions (Figures 1 and S3) and corpus callosum (reported in the Table S2) were defined using the Desikan-Killiany atlas provided in FreeSurfer 5.3.0 (see below for FreeSurfer methods). Basal forebrain regions (CH1/2, CH3, and CH4p; Figures 2 and S2) were defined as previously described.<sup>33</sup> The EC, CC and basal forebrain atlas regions were warped onto individual subject MRIs using Advanced Normalization Tools (ANTS).<sup>68</sup> For all remaining regions reported (Figure 1; Table S2) we generated probabilistic ROIs using our in-house probabilistic ROI atlas. In brief the atlas was generated as follows: 34 regions were manually hand-drawn onto 18 MRIs by experienced technicians guided by brain atlases<sup>69,70</sup> and published reports<sup>71,72</sup> as previously described.<sup>73</sup> Each template was registered to the target MRI using the Automatic Registration Toolbox (ART).<sup>74</sup> Regional labels for each voxel were then determined by evaluating the percentage of the 18 brains that were labeled at that region. The probabilistic labels were used in the calculation of the regional time-activity curves (TACs). Final ROI placement was confirmed by visual inspection before proceeding.

#### Partial volume correction of human PET images

Partial volume effects were corrected using the Iterative Yang technique<sup>75,76</sup> from the PETPVC Toolbox.<sup>77</sup> Instead of calculating the regional mean values via the geometric transfer matrix, the values are estimated from the PET data itself. The Yang correction is applied, and the mean value estimates are recalculated, iteratively, 10 times. The partial volume corrected PET images were then fit for subsequent analyses.

#### [<sup>18</sup>F]VAT distribution volume quantification

To quantify tracer binding, time activity curves from partial volume corrected images along with the arterial input function were analyzed by using a standard 2-Tissue Compartment Model.<sup>78</sup> Subsequent analyses compared the primary outcome measure, distribution volume ( $V_T$ ), a measure of the total amount of radioligand in the tissue compared to the amount available in the blood.<sup>78</sup> Outcomes were log-transformed to stabilize region-wise variance and to fulfill normality assumptions of subsequent model analyses. Hemispheres were plotted and considered individually.

#### FreeSurfer processing of human MRI images

Using MP-RAGE images, cortical thickness and volume were quantified for 34 left and 34 right hemisphere regions defined by the Desikan-Killiany atlas using FreeSurfer 5.3.0 (<http://surfer.nmr.mgh.harvard.edu/>). Freesurfer processing steps include

skull-stripping, Talairach transformation, subcortical gray/white matter segmentation, intensity normalization, gray/white matter tessellation, topology correction, and intensity gradient based surface deformation to generate gray/white and gray/cerebrospinal fluid surface models. The resulting surface models were then inflated and registered to a spherical surface atlas, allowing parcellation of cortical regions of interest. The final outcomes generated were regional entorhinal cortical thickness and volume (Table S1) computed by averaging the white matter-to-pial surface distance at all vertices within the region (CT) or summing the total volume of the region. FreeSurfer EC ROIs were also used for PET analysis (see above).

#### **Human diffusion MRI image analysis**

All T1 and diffusion images were examined for common artifacts such as ghosting and ring-motion using a standardized examination procedure. Diffusion MRI images were loaded into DSI Studio and converted into '.src' files after correction for eddy currents, motion, and phase distortion. Images were reconstructed using Q-space diffeomorphic reconstruction (QSDR) to the adult human template image at 2mm resolution with a 1.25 sampling length ratio for resolution of fiber tracts and fiber orientation. Regions of interest were defined using previously described basal forebrain subregion atlases,<sup>33</sup> and the FreeSurfer entorhinal cortex region. Automated, regional tractography was conducted by setting the MS/DB region as the seed and the entorhinal cortex as End. Diffusion metrics were exported from the visualized tracts for each participant and group metrics were calculated thereafter. The diffusion tensor metrics (FA, MD, AD, etc) were calculated using images with b values = 1000.

#### **Mouse cell counts**

Tissue imaging was conducted on an Olympus wide-field slide-scanner microscope at 20 $\times$  magnification (VS-120 and VS-200 systems, Z-step = 5  $\mu\text{m}$ ), or an Olympus laser scanning confocal at 40 $\times$  magnification (Z-step = 1um). Images were cropped using Olympus VSDesktop, and converted to '.ims' files using the Imaris file converter. Using intensity-based thresholding and filtered by size, the 'Spots' feature was used to identify cFos+ cells within the 3D image. Using intensity based thresholding and filtered by size, the 'Surfaces' feature was used to identify ChAT+ cells within the 3D image. After identification of signal objects (cFos or ChAT+ cells), channels were masked to remove background. For colocalization analysis, masked channels were loaded into the co-localization tab within IMARIS and a new channel was created to include only colocalized pixels. This channel was then evaluated over the raw image and counted using the spots feature to identify colocalized cells.

#### **Mouse terminal field quantification**

To quantify terminal field density, images were collected on an Olympus laser scanning confocal at 40 $\times$  magnification with Z acquisition over a 50um slice (Z-step = 1um). Images were loaded into ImageJ for further analysis. In ImageJ, images were split into individual channels, and the green channel was used for subsequent analyses. Images were then maximum-intensity-projected (MIP) to z-project across the optical sections. The images, in grey-scale, were then evaluated for grey-level value that served as threshold for signal vs. background (noise). Images were then cropped to equal ROIs using the crop to ROI function in ImageJ. Cropped images were saved as TIFs for subsequent processing. Next, cropped images were loaded into MATLAB2018 and binarized (all background pixels were set to zero and all signal pixels were set to 255). Number of pixels in both background and signal groups was determined and the ratio of these was used as the final measure for terminal field density ratio.

#### **Mouse *in vivo* electrophysiology analysis**

Data was thresholded to remove breathing and heartrate signal. Extracellular recordings were sorted offline using the Offline Sorter (Plexon Inc., Dallas, TX). Features of the waveforms were extracted and individual units were demarcated by manually identifying clusters of waveforms in a 2-dimensional feature space of spike properties.<sup>79</sup> The quality of each sort was rated according to isolation distance between clusters. Only recordings of high sort quality, with less than 5% overlap with other clusters, were used for further analysis. Firing rate and inter-spike interval are examined between groups. Single unit recordings were then further analyzed using MATLAB.

#### **Mouse behavior analysis**

Behavior videos were loaded into Ethovision XT15. An empty arena frame was gathered to define the analysis sections within the video. The arena area was subdivided into zones that included each of the three objects (Zones 1–3). The arena was additionally subdivided into quadrants (S1-S4). Keypoint tracking of the animal's location was conducted throughout the video using nose, midpoint, and tail detection. Object exploration was defined as having a detection point within 2 cm of the object zone. Analysis profiles quantified time spent exploring Zone 1-3 separately, number of contacts with each zone, total object exploration, distance traveled. Data presented include time spent exploring the familiar vs. novel objects during the behavioral session.

#### **All statistical analysis**

Statistical analyses were done using GraphPad Prism (GraphPad Software Inc., V10, San Diego, CA, USA) or SPSS (IBM, V28 and V29). PET data was log-transformed for subsequent evaluation in linear mixed models. Normality of remaining data was assessed using Shapiro-Wilk and Smirnov-Kolmogorov tests. Data that failed either normality test were analyzed using non-parametric tests. Parametric tests used include generalized linear model (mixed models and ANOVA), and the Welch's t test (for unequal SDs). Non-parametric comparisons were conducted with a Mann-Whitney test. Correlations were computed using Spearman's correlation tests. All boxplots display a median line with a box extending to the 25<sup>th</sup> and 75<sup>th</sup> percentile. Boxplot whiskers extend to min and max of the dataset. Significance values ( $p$  values) are represented on graphs using the following guidelines:  $p \leq 0.05 = *$ ;  $p \leq 0.005 = **$ ;  $p \leq 0.001 = ***$ ;  $p \leq 0.0001 = ****$ .